International Journal of Solids and Structures 300 (2024) 112928

Contents lists available at ScienceDirect

International Journal of Solids and Structures

journal homepage: www.elsevier.com/locate/ijsolstr

Crystal plasticity finite element simulations of nanoindentation and simple compression for yielding of Ta crystals

Sajjad Izadpanah Najmabad [a], Olajesu F. Olanrewaju [b], Siddhartha Pathak [b], Curt A. Bronkhorst [c], Marko Knezevic [a,*]

[a] Department of Mechanical Engineering, University of New Hampshire, Durham, NH 03824, USA
[b] Department of Materials Science and Engineering, Iowa State University, Ames, IA 50011, USA
[c] Department of Mechanical Engineering, University of Wisconsin, Madison, WI 53706, USA

ARTICLE INFO

Keywords:
Microstructures
Nanoindentation
Crystal plasticity
Yield strength
Tantalum

ABSTRACT

Experiments and corresponding crystal plasticity finite element (CPFE) simulations of spherical nanoindentation were performed to determine yield stress under indentation of fifteen Ta single crystals randomly distributed in the orientation space. Agreement between the measured and simulated indentation yield stresses and initial hardening slopes demonstrated accuracy of the model. Moreover, simple compression simulations were performed for the same crystals to study the differences in compressive versus indentation yielding. Ratios of the indentation to compressive yield stress were found to vary with crystal orientation in the range from 2.6 to 3.6. The simulations allowed us to reveal underlying deformation mechanisms accommodating the yielding in indentation and simple compression. It is found that more crystallographic glid mechanisms activate under indentation than simple compression owing to the more complex state of stress and strain in indentation than in compression. Owing to the activation of more glide systems in indentation than in simple compression, the indentation yield stress is less anisotropic than the simple compression yield stress. The modeling framework, simulation setups, results, and insights from the results are presented and discussed in this paper.

1. Introduction

Nanoindentation is an experimental technique used to test mechanical behavior of materials at the microscale (Fischer-Cripps, 2000; Fischer-Cripps and Nicholson, 2004). A harder indenter of known geometry is used to interrogate a softer specimen under load or displacement. The load and displacement of the indenter are measured as it is driven into and withdrawn from the specimen. Several procedures have been developed for inferring material properties from nanoindentation experiments (Beghini et al., 2006; Donohue et al., 2012; Pelletier, 2006; Taljat et al., 1998). Some procedures combine sophisticated finite element (FE) simulations to match raw indentation load–displacement data and corresponding predictions to extract uniaxial elastic–plastic material properties. Such procedures circumvent obtaining indentation stress–strain curves before extracting the uniaxial properties of interest. However, the properties are best extracted from indentation stress–-strain curves, which most clearly resolve the elastic–plastic transition. To this end, a procedure relying on spherical nanoindentation load–displacement data, including both the loading and unloading portions, was found the most successfully in producing meaningful indentation stress–strain curves (Kalidindi and Pathak, 2008; Pathak and Kalidindi, 2015). Compared to sharper indenters, spherical indenters induce relatively smooth stress fields along with larger initial elastic segments transitioning into the initiation of plasticity and then to post-yield behavior allowing to infer the evolution of the mechanical response. Therefore, the obtained indentation stress–strain curves facilitate inferring indentation modulus, indentation yield strength, and initial hardening slope. While these properties are extracted prior to severe changes induced by the indentation over the specimen, they reflect an average response of the material in the indentation zone. As such, these properties cannot be equivalent to the simple/uniform tension/compression stress–strain response.

Body-centered-cubic (BCC) refractory metals are used in extreme thermal and mechanical conditions in applications such as missile bodies, anti-armor systems, space vehicle components like vanes and nozzles, aircraft structural components like engine parts, heat treating

* Corresponding author at: Department of Mechanical Engineering, University of New Hampshire, 33 Academic Way, Kingsbury Hall, W119, Durham, NH 03824, USA.
E-mail address: marko.knezevic@unh.edu (M. Knezevic).

https://doi.org/10.1016/j.ijsolstr.2024.112928
Received 8 April 2024; Received in revised form 24 May 2024; Accepted 11 June 2024
Available online 14 June 2024

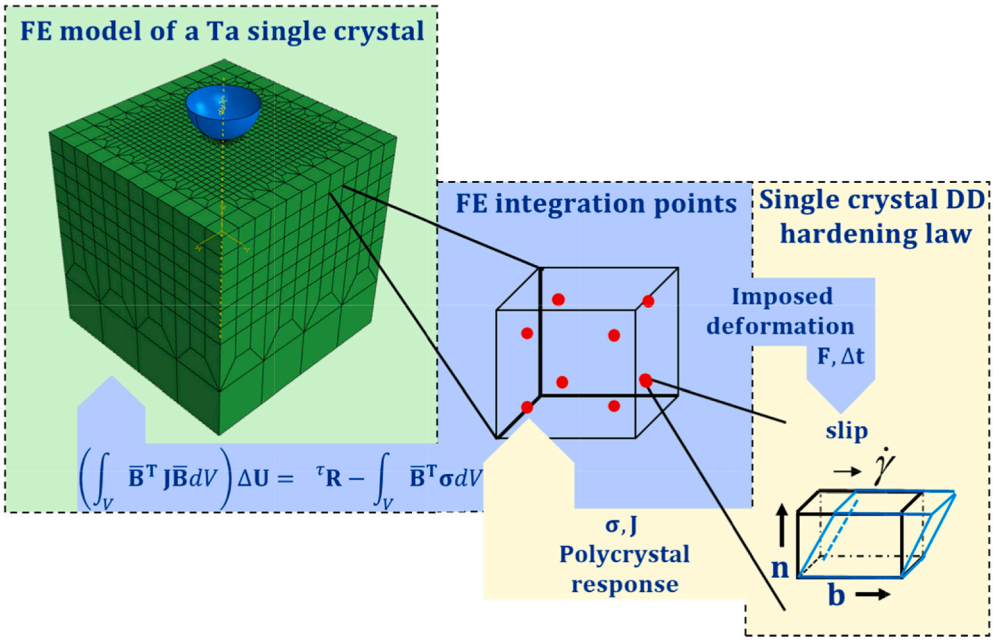

Fig. 1. Schematic of the crystal plasticity modeling framework used to simulate nanoindentation and compression of Ta crystals.

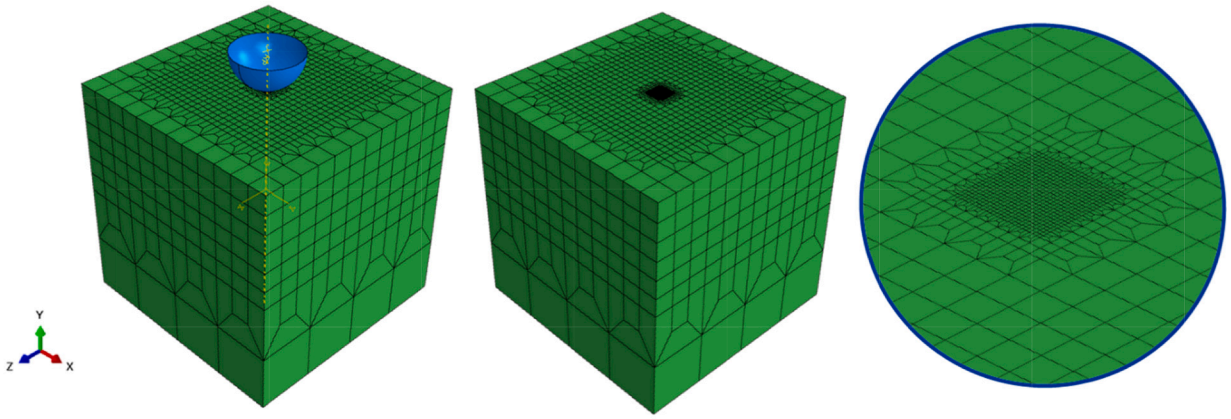

Fig. 2. A setup for the simulations of nanoindentation. The mesh consists of 31,552 C3D8 (continuum 3D 8 nodal) elements. While the bottom face of the mesh is fixed in all directions, the indenter is lowered vertically using the displacement control to facilitate loading–unloading increments of 2 nm.

and glass-melting furnaces, particle accelerators, electronic heat sinks, and even bone replacement implants (Fabricated, 2013; Buckman, 2000; Hesla, 2011; Matsuno et al., 2001; Shields et al., 1999). Tantalum (Ta) is a metal that belongs to the refractory metals group exhibiting a range of desirable properties, such as high melting temperature, conductivity, fracture toughness, ductility, and strength. The deformation behavior of Ta, like other body-centered cubic (BCC) metals, is influenced by crystallographic texture and is sensitive to strain rate and temperature (Bhattacharyya et al., 2015; Bronkhorst et al., 2016; Chen and Gray, 1996; Christian, 1983; Hoge and Mukherjee, 1977; Knezevic et al., 2015). Understanding the localized behavior of the material is of special interest.

Crystal plasticity models have been developed and utilized to physically describe the behavior of metals better than continuum plasticity theories by accounting for microstructure and crystallography of grain-scale deformation mechanisms (Al-Harbi et al., 2010; Asaro and Needleman, 1985; Knezevic et al., 2009; Knezevic et al., 2013a; Knezevic and Kalidindi, 2007; Knezevic et al., 2008b; Kocks and Mecking, 2003; Kocks et al., 1998; Shaffer et al., 2010). Such theories facilitate a deeper understanding of the plasticity of polycrystalline metals and improve accuracy of the plasticity simulations compared to the more commonly used phenomenological plasticity models (Ardeljan et al., 2015b; Fast et al., 2008; Feng et al., 2020; Knezevic et al., 2014c; Knezevic et al., 2008a; Mathur et al., 1989; Wu et al., 2007; Zecevic et al., 2017; Zecevic et al., 2021; Zecevic and Knezevic, 2017). The present paper is concerned with evaluating a crystal plasticity finite element (CPFE) model in capturing yielding of Ta dependent on crystal orientation. Therefore, the deformation response upon indentation and simple compression (SC) can be better understood and predicted with knowledge of crystallography of the deformation mechanisms.

This work combines experiments and corresponding crystal plasticity finite element (CPFE) simulations of spherical nanoindentation in order to determine yield stress under indentation of fifteen Ta single crystals randomly distributed in the orientation space. To this end, a finite element model is developed for the simulation of elastic–plastic spherical indentation involving a rigid indenter and a flat deformable specimen of Ta single crystal. Moreover, SC simulations were performed for the same crystals to study the differences in compressive versus indentation yielding. The model parameters were calibrated using a flow curve obtained in simple tension (ST). Initial microstructure and texture

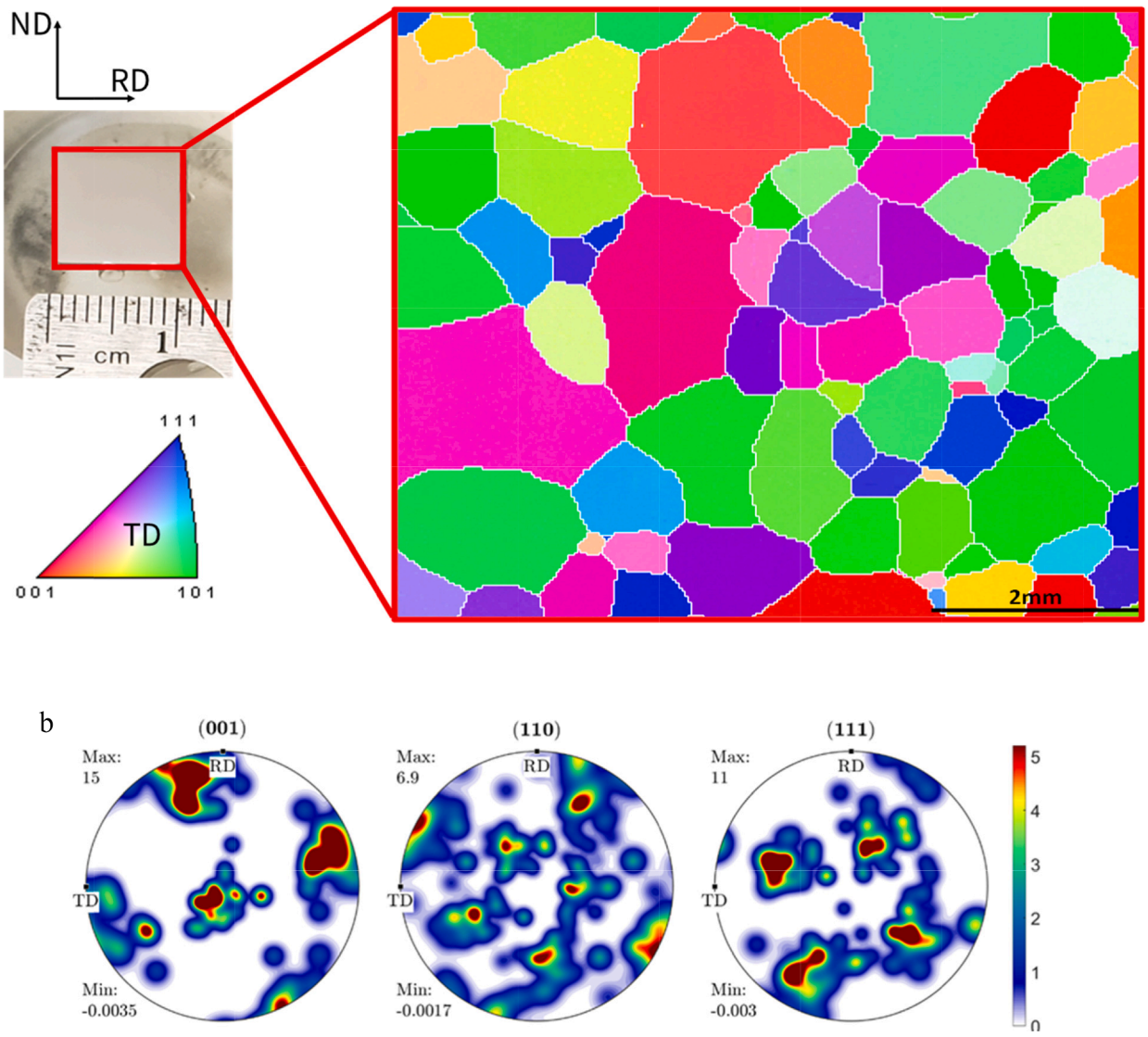

Fig. 3. (a) An inverse pole figure (IPF) map showing the initial grain structure in the annealed Ta plate. (b) Pole figures showing texture of the annealed Ta plate.

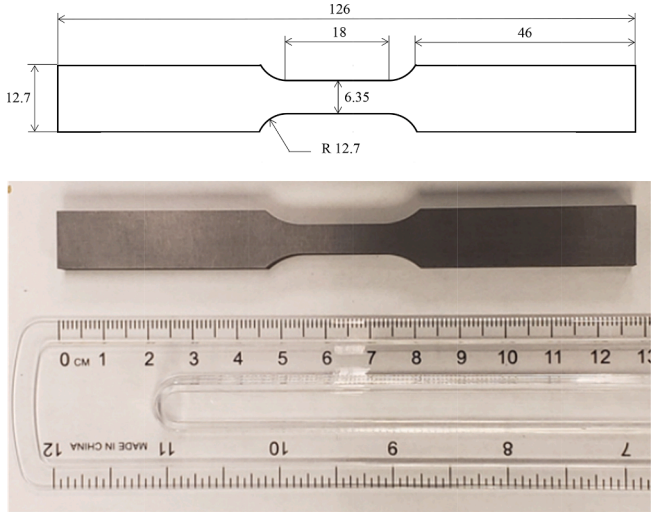

Fig. 4. Drawing of the uniaxial tension specimen in millimeters. The thickness of the specimen was 6.35 mm. Photograph of the specimen.

were characterized using electron backscattered diffraction (EBSD). The simulation results are used to specifically address and discuss several phenomena. Given that the stress/strain fields induced by the indentation are different from those in SC being much more inhomogeneous in the indentation test, we seek to determine the ratios in the properties extracted from indentation stress–strain curves and SC stress–strain curves. Moreover, the underlying deformation mechanisms accommodating the yielding in indentation and SC are determined and the activities discussed. The levels of anisotropy originating from the activation of different glide systems in indentation and in SC are also revealed and discussed. The modeling framework, simulation setups, results, and these insights from the results are presented and discussed in this paper.

2. Modeling framework and simulation setups

This section summarizes the finite deformation CPFE model relevant to the study and simulation setups. Salient kinematics are described in appendix A for completeness, while the hardening law used within the CPFE model and the FE mesh and boundary conditions for simulating spherical indentation are described below. The CFPE model was originally developed in (Kalidindi et al., 1992) and advanced for advanced hardening laws in (Ardeljan et al., 2016a; Feather et al., 2019; Feather

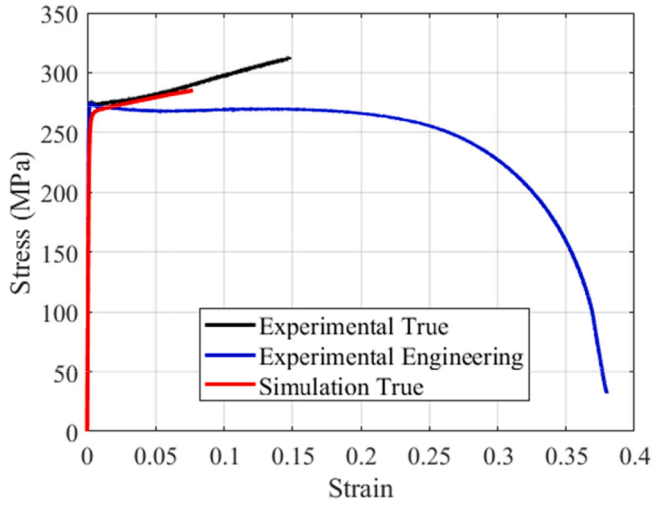

Fig. 5. Comparison of measured and simulated true stress – true strain response in simple tension of annealed Ta along the RD under quasi-static strain rate conditions at room temperature. The simulation was used to establish the model parameters. The experimental engineering stress – engineering strain curve is also plotted to observe the post-necking behavior of the material.

Table 1
Dislocation density-based hardening law parameters adjusted for Ta.

$\tau_0[MPa]$	$k_1[m^{-1}]$	g	$D[MPa]$	q	$\rho_0^s[m^{-2}]$	$\hat{b}[\text{Å}]$	χ
202	0.9E + 08	0.005	305	4	1.0E + 12	3.3058	0.9

et al., 2021; Zecevic et al., 2019). In the description that follows and in the appendix, tensor quantities are denoted using bold letters; tensor components and scalars are italicized and not bold; s, and α are used to denote slip systems and slip modes, respectively; $\bullet$ is used for a dot product, while $\otimes$ is used for a tensor product. N^{sl} is the total number of slip systems.

A dislocation density-based (DD) hardening law for obtaining τ_c^s is implemented within the CPFE. This formulation of the hardening law was used to compute the evolution of slip resistances as a function of strain and strain rate in many other works (Ardeljan et al., 2017; Beyerlein and Tomé, 2008; Knezevic and Beyerlein, 2018; Knezevic et al., 2012; Knezevic et al., 2014b). To estimate the resistance required to trigger slip, we consider the contributions of the following terms: a friction stress τ_0^s, a forest dislocation interaction stress τ_{for}^s and a dislocation substructure interaction stress τ_{sub}^α (Ardeljan and Knezevic, 2018; Knezevic et al., 2013c):

$$\tau_c^s = \tau_0^\alpha + \tau_{for}^s + \tau_{sub}^\alpha \tag{1}$$

Furthermore, the individual behavior of τ_{for}^s and τ_{sub}^α is determined by the evolution of the dislocation densities that consist of forest ρ_{for}^α and substructure ρ_{sub}^α dislocations. For this purpose, a Taylor-like law is used to represent these relationships for each dislocation type. These are expressed as (Ardeljan et al., 2016b):

$$\tau_{for}^s = \chi b^\alpha \mu^\alpha \sqrt{\rho_{for}^s} \tag{2}$$

$$\tau_{sub}^\alpha = 0.086 \mu^\alpha b^\alpha \sqrt{\rho_{sub}} log\left(\frac{1}{b^\alpha \sqrt{\rho_{sub}}}\right) \tag{3}$$

Here χ is a dislocation interaction parameter, while 0.086 is a mathematical parameter that insures that Eq. (3) compensates the Taylor law at low dislocation densities (Capolungo et al., 2009). The initial material state corresponds to an annealed state. The value of stored forest density ρ_{for}^α changes according to competition between the rate of storage/generation and the rate of dynamic recovery/removal (Ardeljan et al., 2015a):

$$\frac{\partial \rho_{for}^s}{\partial \gamma^s} = \frac{\partial \rho_{gen,for}^s}{\partial \gamma^s} - \frac{\partial \rho_{rem,for}^s}{\partial \gamma^s} = k_1^\alpha \sqrt{\rho_{for}^s} - k_2^\alpha(\dot{\epsilon}, T)\rho_{for}^s, \Delta\rho_{for}^s = \frac{\partial \rho_{for}^s}{\partial \gamma^s}|\Delta\gamma^s| \tag{4}$$

In Eq. (4) k_1^α is a coefficient for the rate of dislocation storage because of statistical trapping of gliding dislocations and k_2^α is the coefficient for the rate of dynamic recovery by thermally activated mechanisms. The second coefficient can be determined by this relationship (Zecevic and Knezevic, 2015):

$$\frac{k_2^\alpha(\dot{\epsilon}, T)}{k_1^\alpha} = \frac{\chi b^\alpha}{g^\alpha}\left(1 - \frac{kT}{D^\alpha b^3} ln\left(\frac{\dot{\epsilon}}{\dot{\epsilon}_0}\right)\right) \tag{5}$$

where k, $\dot{\epsilon}_0$, g^α and D^α are respectively Boltzmann's constant, a reference strain rate (taken here to be 10^7 s^{-1}), an effective activation enthalpy and a drag stress. Lastly, the increment in substructure development can be related to the rate of dynamic recovery of all active dislocations as (Zecevic et al., 2020):

$$\Delta\rho_{sub} = \sum_s q b^\alpha \frac{\partial \rho_{rem,for}^s}{\partial \gamma^\alpha}|\Delta\gamma^s| \tag{6}$$

where q is a rate parameter that determines the fraction of an s-type dislocations that do not annihilate but become substructure dislocations.

The modeling framework explained above to simulate spherical nanoindentation tests is schematically presented in Fig. 1.

The computational mesh and setup employed in this study is depic-

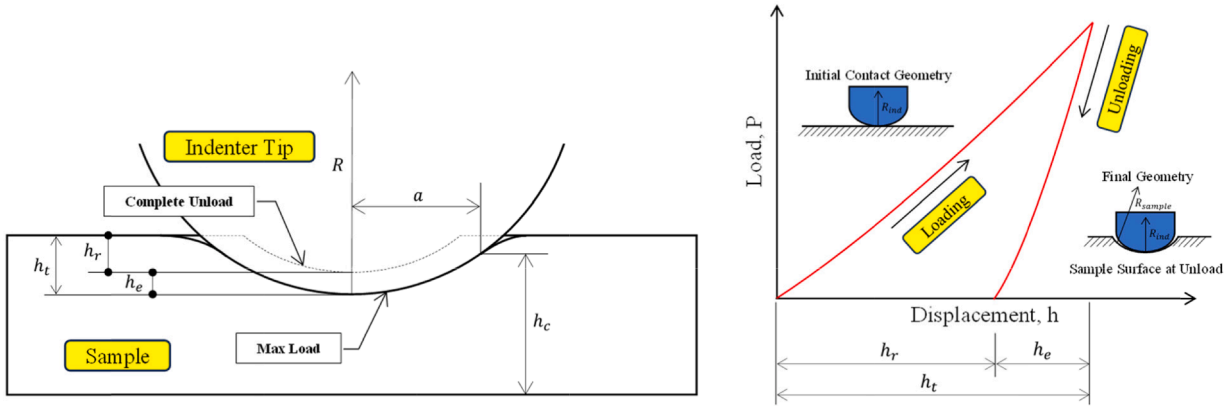

Fig. 6. Schematics of spherical nanoindentation (left) and indentation load–displacement curve along with the initial and final contact geometries (right).

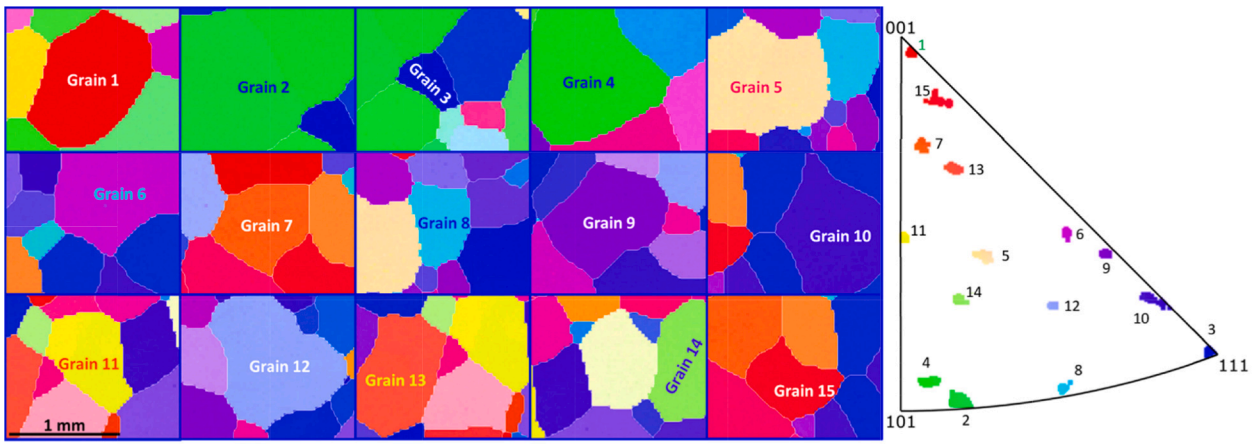

Fig. 7. IPF maps of the 15 grains for nanoindentation and their location in the standard IPF triangle. The sample axis is perpendicular per map and is TD for the grains numbered from 1 to 4 and ND for the grain numbered from 5 to 12.

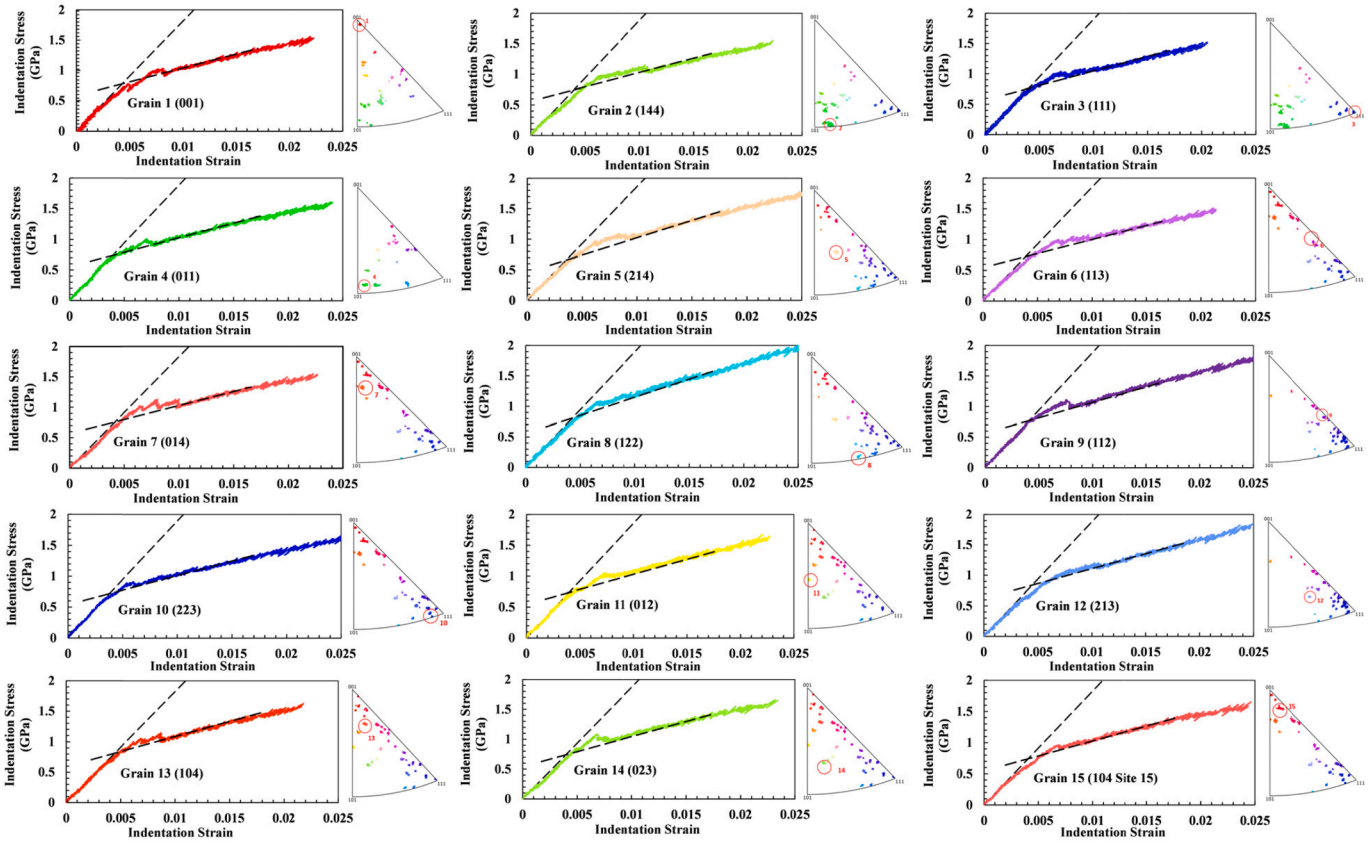

Fig. 8. Indentation stress – indentation strain based on the measured load – displacement data for the 15 grains. Intersections between the elastic slope black lines and the initial hardening slope black lines are taken as yield stresses.

ted in Fig. 2. The numerical model consists of two three-dimensional parts: (1) an elastic–plastic deformable sample and (2) a rigid hemispherical indenter with a radius of 150 nm, consistent with the experimental dimensions. The deformable part was meshed using three-dimensional linear continuum elements with eight nodes (C3D8 in Abaqus notation). The sample's dimensions measure $1mm \times 1mm \times 1mm$ as selected to confine the stress–strain fields within the indentation zone. The deformable model incorporates a total of 31,552 elements, with 20,480 elements situated within the indentation zone. Consequently, the indentation zone is divided into three regions, as depicted in Fig. 2, enabling a progressively higher mesh density closer to the indenter-sample contact surface. This partitioning strategy permitted the application of finer meshing in regions expected to exhibit higher stress and strain gradients within the sample. The aspect ratio of all elements was approximately 1. The Coreform Cubit software facilitated the generation of this high-quality mesh, offering localized mesh refinement beneath the indenter tip zone while preserving node connectivity (Feather et al., 2020; Weiss and Knezevic, 2024). The mesh quality assessment involved comparing simulated load–displacement curves with experimental data. The authors' observation sustained that a low-quality mesh produces oscillations in load–displacement curves. The mesh was refined to eliminate such unrealistic oscillations. In

Table 2
Measured and simulated values of indentation elastic slope, indentation yield stress, and Young's modulus for the 15 Ta crystals. The last two columns report the relative errors in percentage for both indentation elastic slope and indentation yield stress.

Grain #	Orientation	Simulation E_{ind} (GPa)	Experiment E_{ind} (GPa)	Simulation σ_{ind} (GPa)	Experiment σ_{ind} (GPa)	Φ_1, Φ, Φ_2	Error (%)$Error = ABS\left(\frac{E_{exp} - E_{sim}}{E_{exp}}\right) \times 100$	Error (%)$Error = ABS\left(\frac{Y_{exp} - Y_{sim}}{Y_{exp}}\right) \times 100$
Grain 1	**001**	180	181.3 ± 0.21	0.74	0.76 ± 0.014	335.92°, 1.91°, 32.57°	0.717	2.631
Grain 2	**144**	188	188.2 ± 0.12	0.76	0.80 ± 0.015	81.11°, 44.41°, 8.27°	0.106	5.0
Grain 3	**111**	190	190.3 ± 0.12	0.78	0.84 ± 0.027	172°, 53.40°, 44.63°	0.157	7.142
Grain 4	**011**	188	188.3 ± 0.13	0.76	0.78 ± 0.007	89.72°, 41.25°, 85.57°	0.159	2.948
Grain 5	**214**	185	186.3 ± 0.16	0.79	0.80 ± 0.006	107.25°, 27.78°, 69.5°	0.697	1.25
Grain 6	**113**	184	185.3 ± 0.09	0.78	0.79 ± 0.011	187.39°, 30.04°, 49.76°	0.701	1.265
Grain 7	**014**	182	183.0 ± 0.36	0.75	0.77 ± 0.007	214.77°, 13.41°, 10.48°	0.546	2.597
Grain 8	**122**	188	189.3 ± 0.15	0.80	0.83 ± 0.011	202.58°, 46.53°, 24.94°	0.686	3.614
Grain 9	**112**	187	188.0 ± 0.33	0.77	0.79 ± 0.016	183.74°, 35.21°, 43.26°	0.531	2.531
Grain 10	**223**	189	189.4 ± 0.07	0.79	0.82 ± 0.014	144.99°, 42.97°, 43.61°	0.211	3.6585
Grain 11	**012**	184	185.5 ± 0.12	0.75	0.78 ± 0.001	72.91°, 23.78°, 1.15°	0.808	3.846
Grain 12	**213**	186.5	187.8 ± 0.09	0.79	0.81 ± 0.003	311.03°, 36.59°, 60.58°	0.692	2.469
Grain 13	**104**	182	182.6 ± 0.15	0.74	0.77 ± 0.019	284.46°, 14.99°, 69.53°	0.328	3.896
Grain 14	**023**	185	186.7 ± 0.20	0.77	0.79 ± 0.011	177.13°, 31.73°, 11.98°	0.910	2.531
Grain 15	**104**	181	182.6 ± 0.07	0.76	0.78 ± 0.004	247.06°, 8.35°, 63.26°	0.876	2.564

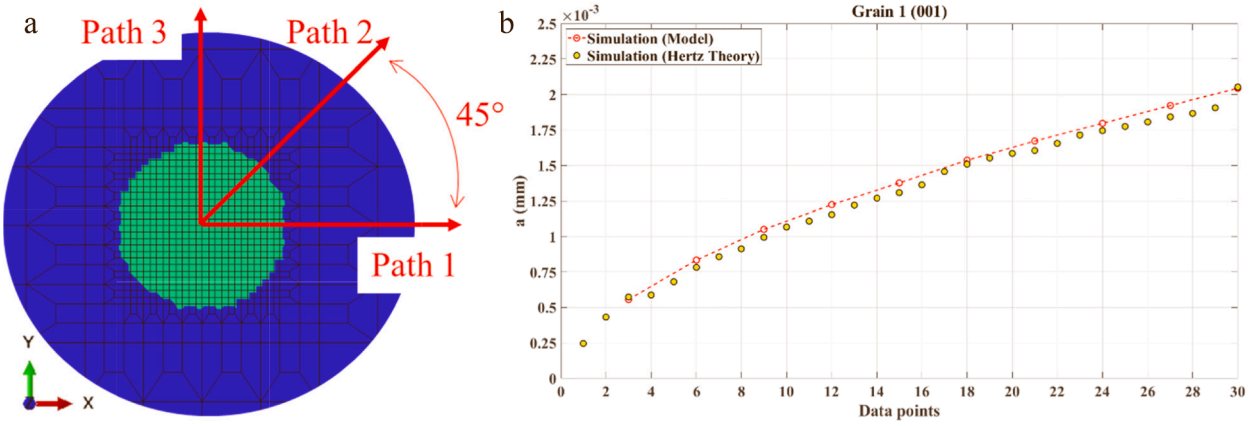

Fig. 9. (a) Projection of in-contact (green) and not-in-contact (blue) contours based on the contact status parameter (CSTATUS) in Abaqus at an instant during the indentation simulation of Grain 1. (b) Comparison between the CSTATUS in Abaqus determined curve as an average of three directions and analytical curve based on the Hertz theory (Donohue et al., 2012).

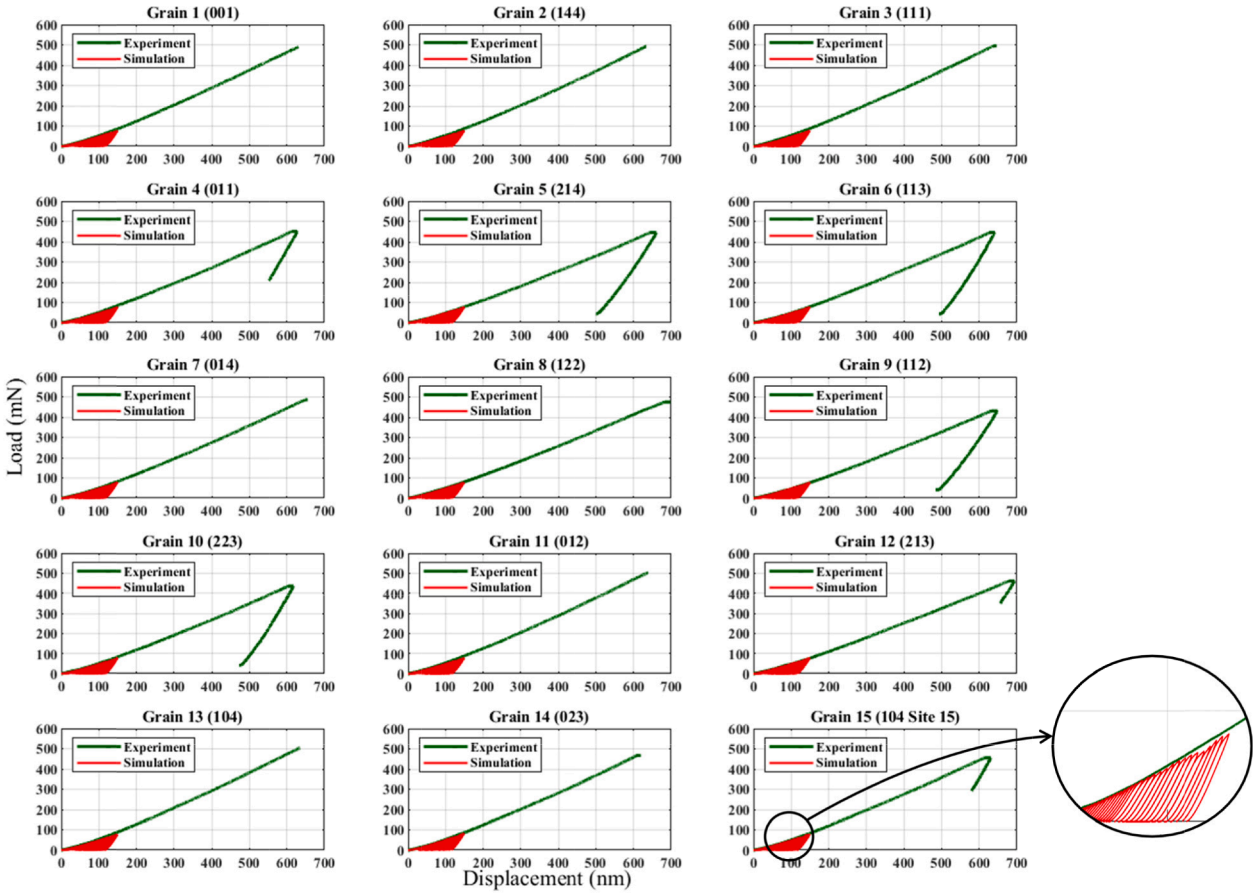

Fig. 10. Experimentally measured and simulates load – displacement curves for the 15 Ta crystals.

simulations, a final mesh underwent multiple loading–unloading cycles, which was necessary for recovering the indentation stress–strain curves.

The contact condition between the sample and indenter were defined as frictionless, hard surface-to-surface contact. The indenter's reference point was fixed in all degrees of freedom except the Y-direction (the indentation direction), allowing for a displacement boundary condition in this specific direction. Additionally, the node set at the bottom surface of the sample along the Y-direction is constrained but the lateral surfaces of the deformable sample remained free throughout the simulation. Both the indenter displacement and the total applied force on the sample were recorded at every time increment during the simulation.

The indenter displacement was initially set to 1*nm* up to 80*nm*, followed by a change to 3*nm* until the end of simulations. The change from 1 nm to 3 nm was to improve computational efficiency without appreciably influencing the results. The 1 nm displacement increments at the start of simulations, where the elastic deformation prevails, allowed to accurately capture the elastic slope, yield stress, and initial hardening slope. The rest of the displacement increments were used to capture the subsequent hardening meaning that the change from 1 nm to 3 nm did not appreciably influence the results but only accelerated the simulations.

3. Results

This section presents results of the work beginning from the material characterization to model calibration to finally nanoindentation experiments and simulations.

3.1. Material characterization

High purity (99.995 %), polycrystalline Ta was used for this research. The samples were annealed at a relatively high temperature of 1700 °C (0.6 T_M for Ta) for 24 h under vacuum atmosphere to prevent spontaneous oxidation, resulting in large (few millimeters) sized grains which provide ample space for nanoindentation testing. The samples were prepared for electron backscattered diffraction (EBSD) and nanoindentation studies by mounting them in epoxy, followed by successive mechanical grinding and polishing steps with silicon carbide (SiC) abrasive papers and diamond suspensions, respectively. Finally, they were vibratory polished in a 0.05 μm colloidal silica on a Buehler vibratory polisher for 48 h. Vibratory polishing is a vital final step needed to produce smooth, strain free surfaces for EBSD and indentation measurements (Pathak et al., 2009a,2009b).

Subsequently the crystallographic orientation of each grain in the Ta samples was obtained from the automated indexing of EBSD patterns obtained on the FEI Teneo field emission scanning electron microscope equipped with Oxford energy dispersive and backscattered electron (EDS/EBSD) detectors using the Aztec Crystal Oxford Software at a magnification of 20X and step size of 5 μm. Fig. 3 shown the grain structure and texture in the initial material.

3.2. Model calibration for Ta

Before simulating the spherical nanoindentation tests, we calibrate the hardening law parameters using a flow curve recorder in ST for Ta under a quasi-static strain rate at room temperature. Fig. 4 shows a tension specimen to test the material. Three tests were performed to verify the repeatability and no appreciable differences were detected.

In all simulations, Ta is assumed to deform by $\{1\bar{1}0\}\langle 111\rangle$ and $\{11\bar{2}\}\langle 111\rangle$ slip modes/families. The initial slip resistance and hardening parameters of both slip families are considered to be the same. Fig. 5 shows the prediction of the model compared to the experimental

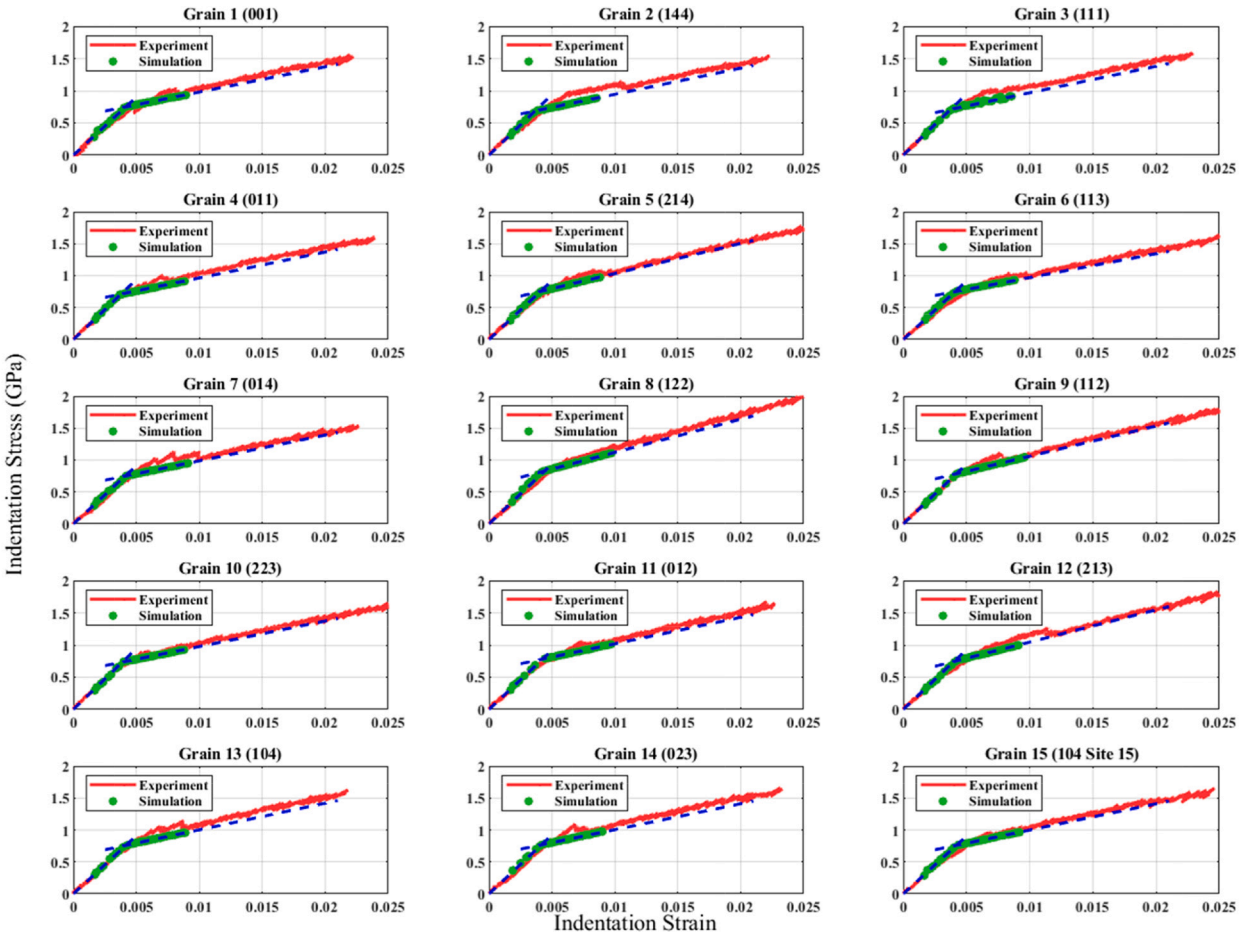

Fig. 11. Comparison of experimental and simulated indentation stress – indentation strain curves based on the corresponding load – displacement data for the 15 grains. Intersections between the elastic slope blue lines and the initial hardening slope blue lines are simulated yield stresses.

stress–strain curve. The experimental data is presented in the form of true and engineering curves to better appreciate the behavior of the annealed Ta. Evidently a good fit of the data is obtained especially for the yield stress and the initial hardening slope which are the focus of this study.

In order to capture the response, the following model parameters are fit (Savage et al., 2021; Veasna et al., 2023): initial slip resistance or critical resolved shear stress, τ_0^α, trapping rate coefficient, k_1^α, activation barrier for depinning, g^α, drag stress, D^α, and an additional rate coefficient q^α. The fitting procedure consisted of varying τ_0^α to fit yield stress. Next, k_1^α, was adjusted such that the initial hardening slope was reproduced. Next, g^α and D^α are adjusted to match the rest of the hardening behavior. Finally, q^α is adjusted to also capture the hardening behavior.

The calibrated parameters were established using a cubic FE model consisting of 64 three-dimensional continuum elements with eight nodes (C3D8), akin to those used in the nanoindentation simulations. All elements had initially an aspect ratio of 1. The model was initialized with 3072 equally weighted crystal orientations representing the measured texture. Every integration point embedded 6 different equally weighted crystal orientations from the total of 3072. The response of the 6 crystal orientations is homogenized using the Taylor model (Weiss et al., 2024; Weiss et al., 2023). To replicate the uniaxial tension condition, displacement was applied in the RD direction, while the lateral surfaces were stress free.

Table 1 presents the calibrated parameters of Ta for dislocation density-based hardening law. The crystal elastic constants for Ta are $C_{11} = 268.5GPa$, $C_{12} = 159.9GPa$, $C_{44} = 87.1GPa$.

3.3. Spherical nanoindentation experiments and stress-strain analysis

Fig. 6 shows the schematic view of the indentation process along with the parameters used in the equations.

The nanoindentation tests were carried out using the MTS-XP and KLA iMicro systems with the continuous stiffness measurement option. A spherical indenter tip of 150 μm radius (manufacturer Synton-MDP, Switzerland) was used for the measurements. The tests were carried out in load-controlled mode with a specified maximum displacement of 700 nm for all samples. At least 10 indents were analyzed for each grain/region studied in this work. The importance of considering connections or the base of the indentation instrument and the environment in modeling was discussed in (Xu et al., 2022; Zhang et al., 2016) for micro-pillar testing. While the connection to the base can be important in micro-pillar testing experiments, it is less of a concern in the indentation experiments, especially for small depths. The indentation experiments were conducted under ambient conditions and therefore any effects of environment and temperature were not considered. Moreover, since Ta as a refractory metal, any temperature related effects would only be manifested at significantly higher temperatures ($\geq 0.3\ T_m$, where $T_m =$ 3290 K, 3017 °C is the melting point of Ta in Kelvin). The indentation experiments can be affected by Ta oxide which can form on the Ta surface at lower elevated temperatures, but the effect is minimal at room temperature. Finally, our experimental work relies on a protocol involving the determination of the zero point for the initial elastic segment of the spherical indentation experiments (Kalidindi and Pathak, 2008). This zero-point correction ensures that any effects caused by the presence of a thin (~nm) oxide layer can be accounted for during the

Table 3
Yield stress and Young's modulus determined by simulating SC for the 15 Ta crystals.

Grain #	Orientation	Φ_1, Φ, Φ_2	YS (MPa)	Young's Modulus $E = 1/S_{1111}$ (GPa)
Grain 1	001	335.92°, 1.91°, 32.57°	272.6	152.5
Grain 2	144	81.11°, 44.41°, 8.27°	243.3	201.4
Grain 3	111	172°, 53.40°, 44.63°	243.3	200.7
Grain 4	011	89.72°, 41.25°, 85.57°	244.8	200.6
Grain 5	214	107.25°, 27.78°, 69.5°	259.4	178.5
Grain 6	113	187.39°, 30.04°, 49.76°	235.9	182.1
Grain 7	014	214.77°, 13.41°, 10.48°	235.2	203.5
Grain 8	122	202.58°, 46.53°, 24.94°	205.6	209.9
Grain 9	112	183.74°, 35.21°, 43.26°	242.8	201.2
Grain 10	223	144.99°, 42.97°, 43.61°	225.3	183.9
Grain 11	012	72.91°, 23.78°, 1.15°	268.4	184.6
Grain 12	213	311.03°, 36.59°, 60.58°	213.9	191.9
Grain 13	104	284.46°, 14.99°, 69.53°	278.6	160.2
Grain 14	023	177.13°, 31.73°, 11.98°	273.7	153.5
Grain 15	104	247.06°, 8.35°, 63.26°	237.3	201.6

initial contact of the indenter tip with the interrogated material (Pathak et al., 2009a). Given these arguments and that the CPFE model was calibrated to match the experimental conditions as accurately as possible for only the initial (~150 nm) portion of the indentation experiments, the consideration of the environment and connections or the base of the indentation instrument would be excessive. Further details of nanoindentation tests, and the data analysis protocols used to obtain indentation stress–strain curves can be found in prior reports (Pathak et al., 2009b), and are briefly summarized below.

The load–displacement and stiffness measurements were converted into meaningful stress–strain curve using protocols described in prior reports (Pathak and Kalidindi, 2015; Pathak et al., 2009b). These protocols are based on Hertz theory and can be explained as a two-step procedure. The first step includes the evaluation of the effective point of contact for a given data set in which the initial elastic loading segment is consistent with Hertz theory (Hertz, 1896). These protocols (Kalidindi and Pathak, 2008) demonstrate that the zero point can be conveniently determined using the following equation for the initial elastic segment in a frictionless, spherical indentation:

$$S = \frac{3P}{2h_e} = \frac{3\left(\widetilde{P} - P^*\right)}{2\left(\widetilde{h}_e - h^*\right)} \tag{7}$$

where $\widetilde{P}$, $\widetilde{h}_e$, and S are the measured load signal, the measured displacement signal, and the continuous stiffness measurement (CSM) signal in the initial elastic loading segment from the machine, respectively, and P^* and h^* denote the values of the load and displacement values at the point of effective initial contact (i.e., P^* and h^* are the zero-point corrections needed). Rearrangement of the equation reveals that a plot of $\widetilde{P} - \frac{2}{3}S\widetilde{h}_e$ against S will produce a linear relationship whose slope is equal to $-\frac{2}{3}h^*$ and the y-intercept is equal to P^*. A linear regression analysis can then be performed to identify the point of the effective initial contact (P^* and h^*) very accurately.

In the second step, the values of indentation stress and strain can be calculated by recasting Hertz theory for frictionless, elastic, spherical indentation as

$$\sigma_{ind} = E_{eff}\varepsilon_{ind}, \sigma_{ind} = \frac{P}{\pi a^2}, \varepsilon_{ind} = \frac{4}{3\pi}\frac{h_e}{a} \approx \frac{h_e}{2.4a}$$

$$a = \frac{S}{2E_{eff}}, \frac{1}{E_{eff}} = \frac{1}{\beta}\left(\frac{1-\nu_s^2}{E_s}\right) + \left(\frac{1-\nu_i^2}{E_i}\right), \frac{1}{R_{eff}} = \frac{1}{R_i} + \frac{1}{R_s} \tag{8}$$

where σ_{ind} and ε_{ind} are the indentation stress and indentation strain, a is the radius of the contact boundary at the indentation load P, h_e is the elastic indentation depth, S ($=dP/dh_e$) is the elastic stiffness described earlier, R_{eff} and E_{eff} are the effective radius and the effective stiffness of the indenter and the specimen system, ν and E are the Poisson's ratio and the Young's modulus, and the subscripts s and i refer to the specimen and the indenter, respectively. β is an anisotropic parameter defined in (Vlassak and Nix, 1993, 1994) which is used to account for elastic indentation of anisotropic cubic materials. For cubic crystals, the value of β depends strongly on the crystal lattice orientation and the degree of cubic elastic anisotropy (also known as Zener's ratio A (Meyers and Chawla, 2009) usually defined as $A = 2C_{44}/(C_{11} - C_{12})$, where C_{11}, C_{12}, and C_{44} denote the cubic elastic constants used to define the crystal elastic stiffness in its own reference frame. Tantalum has a body centered cubic structure with a Zener's ratio of $A = 1.56$. Thus from Eq. (16), the value of β for Ta should vary between 0.97–1.03. I.e., for Ta the values of the indentation modulus should range from 181.1 GPa for the (0 0 1) orientation to 190.3 GPa for the (1 1 1) orientation. The measured values of β (range ~ 0.98 to 1.03, i.e. indentation modulus of 181.3 GPa for the (0 0 1) orientation and to 190.4 GPa for the (1 1 1) orientation) from our spherical indentation stress–strain analysis are highly consistent with the predictions from Eq. (16).

Fig. 7 depicts fifteen grain orientations evenly spaced over the inverse pole figure triangle selected for our detailed study of spherical nanoindentation. Fig. 8 shows the indentation stress – indentation strain curves based on the measured load – displacement data for the 15 grains.

3.4. Nanoindentation and simple compression simulations

As already said, the general methodology for converting indentation load–displacement data into stress strain data can be found in (Pathak et al., 2009a,2009; Kalidindi and Pathak, 2008). Like in the experiments, the key equations for obtaining the indentation stress and strain from the simulations are also $\varepsilon_{ind} = \frac{4}{3\pi}\frac{h_e}{a}$ and $\sigma_{ind} = \frac{P}{\pi a^2}$, where h_e is the elastic portion of the displacement as shown in Fig. 6 and P is the load at the peak for each single loading then unloading step. Based on these equations, estimation of the indentation stress and strain necessiates knowledge of the contact area a under the indenter tip. To apply Hertz's theory in these calculations, a should only be calculated from the elastic unloading segments of the load displacement curves using $a = \frac{S}{2E_{eff}}$. Here, S is the stiffness of the unloading portion of the loading–unloading curve and E_{eff} is the effective Young's modulus of the indenter and the specimen system defined using $\frac{1}{E_{eff}} = \frac{1-\nu_s{}^2}{E_s} + \frac{1-\nu_i{}^2}{E_i}$, where E and ν are Young's modulus and Poisson's ratio with the subscripts s and i identifying the specimen and the indenter, respectively. In this study, we take $E_i = 1140GPa$, $\nu_i = 0.07$, and $\nu_s = 0.3$ for all 15 crystals, and E_s is the experimental data given in Table 2 (E_{ind}) like in (Donohue et al., 2012).

As highlighted in (Pathak et al., 2009a,2009; Kalidindi and Pathak, 2008), accurately determining the unloading (elastic) stiffness (S) plays a pivotal role in reliably estimating the contact area. This quantity is essential for computing both indentation stress and indentation strain measures. Also, note that each unloading step provides a single data point for indentation stress strain curves (only one value for both

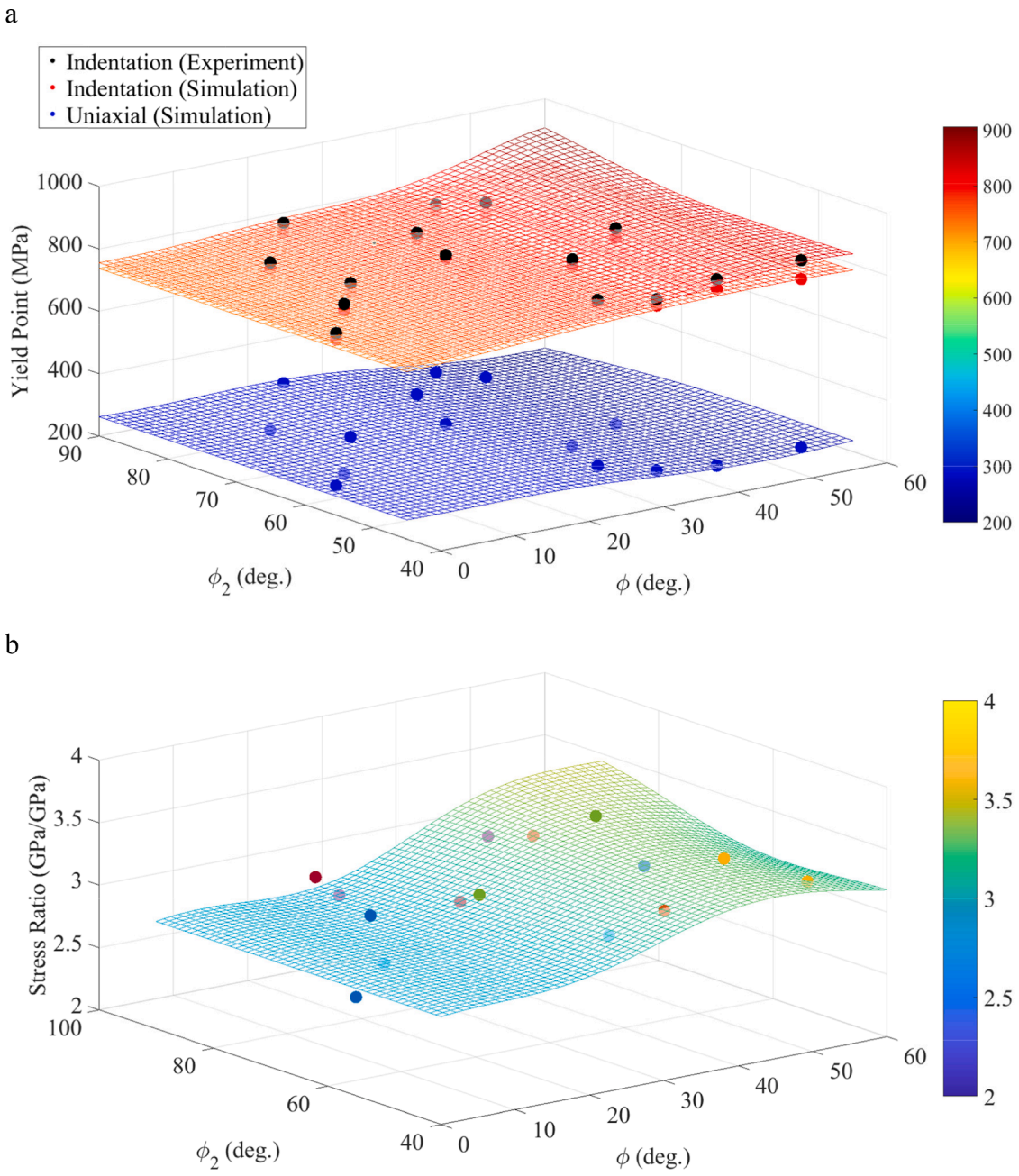

Fig. 12. (a) Surface contour plots in MPa comparing the measured and simulated indentation yield stresses based on the values for the 15 crystal orientations of Ta. Also plotted is a surface of simple compression yield stresses based on the values for the 15 crystal orientations of Ta simulated using two slip modes. (b) A surface plot of the ratio between indentation yield stress and simple compression yield stress based on the values for the 15 crystal orientations of Ta.

indentation stress and indentation strain per unloading). Therefore, it is mandatory to apply a very large number of unloading steps in the simulations to be able to document the accurate evolution of nanoindentation stress vs strain. These unloading segments will be highlighted for grain 15.

The calculation of $S = \frac{3P}{2h_e}$ presents several challenges, emphasizing the critical need to verify the accuracy of estimating the contact area (Donohue et al., 2012). Therefore, to ensure the adequacy of calculated indentation stress and strain data points, the derived values of a determined through the procedure mentioned above (Hertz's theory), are compared with the actual contact area obtained from the FE model for grain 1. The outcomes of this comparison are depicted in Fig. 9. In the figure, simulation (model) represents the contact area values extracted from the FE model (left figure) at different time steps. The good agreement between the two curves verifies the accuracy in the calculation of the contact area. To quantify the result of this comparison and get a better estimation of the overall accuracy, the following equation is used to calculate the error term in percentage:

$$Error(\%) = \frac{\sum_{i=1}^{N} ABS\left(\frac{a_i^{model} - a_i^{Hertz}}{a_i^{model}}\right)}{N} \times 100 \tag{9}$$

In Eq. (9), N is number of data points which is 30. The value of error for calculation of contact area based on this Eq. is 3.87%, which is an acceptable accuracy in the calculation of the contact area evolution.

Fig. 10 displays a comparison between the simulated and experimental load–displacement curves for the 15 Ta crystals. Specifically, the unloading segments are magnified for grain 15 to enhance visibility. The

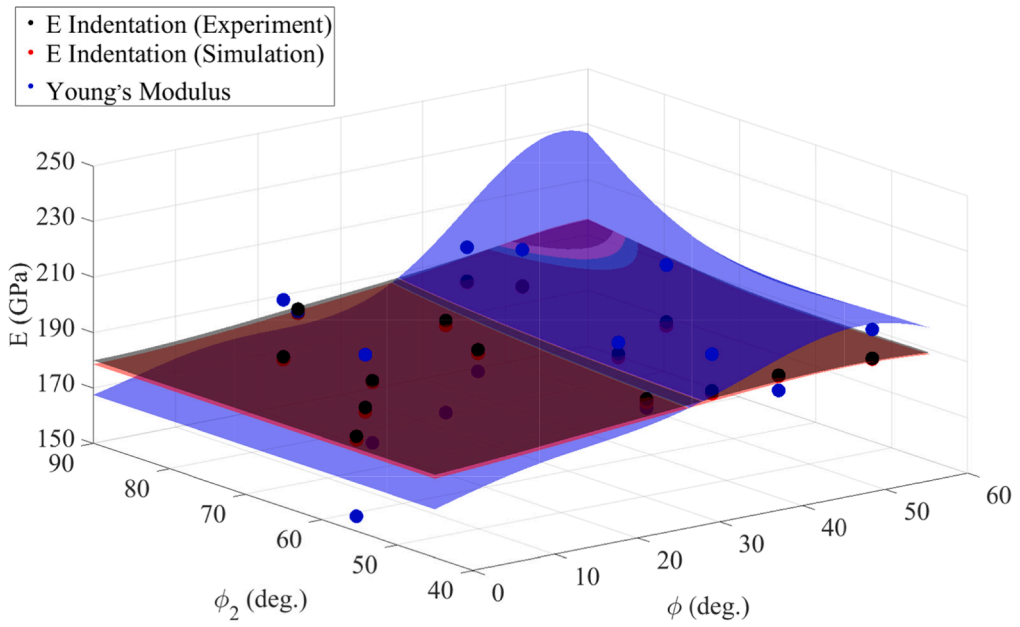

Fig. 13. Surface contour plots comparing the measured and simulated indentation elastic slopes along with Young's modulus based on the values for the 15 crystal orientations of Ta.

figure shows good agreement between the simulations and experiments. Given the study's primary focus on capturing the elastic slope, yield stress, and initial hardening rate per crystal, we limited the simulation range. Instead of extending the load–displacement curves to ~ 600 nm, simulations were terminated at 150 nm. This strategy not only successfully captured the yield stress for all crystals but also notably reduced computational time. Nevertheless, every simulation took about two days using 32 CPUs. Additionally, the zoomed-in section for grain 15 reveals two distinct displacement steps, as previously mentioned. This deliberate approach aimed to generate more data points within the elastic segment of the indentation stress vs. indentation strain curves.

Fig. 11 illustrates the indentation stress vs. indentation strain curves for the 15 crystals, computed using the equations introduced earlier in this section. The calibrated parameters presented in Table 1 were used in these simulations. The calculation of the stiffness parameter, S, involved selecting data points corresponding to loads at each peak before unloading. Subsequently, the slope of the unloading section immediately following the peak point is determined. The methodology for capturing the indentation stress versus indentation strain relationship is outlined in detail in prior works (Weaver and Kalidindi, 2016; Weaver et al., 2016).

The calibrated parameters presented in Table 1 were employed to simulate SC tests for the 15 crystals, primarily aimed at determining the yield stress of the single crystals. The FE model was the same as the one used for parameter calibration, except that the loading is reversed from simple tension to compression and every integration point of the model received the same crystal orientation. Also, Young's modulus is calculated for every crystal. To this end, the elastic compliance tensor is calculated for every crystal and the Young's modulus obtained using $E = 1/S_{1111}$ relationship (Cantara et al., 2019). Table 3 provides a summary of the results from these simulations conducted using the previously described model setup for ST.

Fig. 11 shows a very good alignment between the experimental and simulation results. To quantify the precision of the simulations presented in this figure, the values of elastic slope (E_{ind}) and yield stress (Y_{ind}) for the 15 crystals are presented in Table 2 and compared with the experiments. Additionally, the error percentages for these parameters are calculated and listed in the last two columns of the table. Notably, the maximum error for calculating the indentation elastic slope is nearly 1 %, while for the indentation yield stress, it is approximately 5 %. These findings substantiate the accuracy of simulations in capturing the nanoindentation stress–strain profiles. Moreover, the predictions show that the variation in the response of individual crystals is driven by crystallography. The significant role played by crystal orientation-driven anisotropy was recently discussed for Ta single crystals in (Feng et al., 2022).

Fig. 12a presents a combined illustration of the yield stresses for the 15 Ta crystals through a yield surface-type plot over the orientation space. The figure depicts surface plots representing experimental and simulation results from nanoindentation and SC simulations, facilitating a direct comparison. The yield stresses in SC are notably lower when contrasted with the indentation yield stresses. While the averaged ratio of indentation to compressive yield stresses is about 3.1, the range is approximately from 2.6 to 3.6. The finding is a remarkable result given that computational results of Donohue (Donohue et al., 2012) and Patel (Patel and Kalidindi, 2016, 2017) had postulated a ratio of 2.2 for isotropic elastic–plastic solids. Fig. 12b shows the surface plot of the ratio based on the 15 crystal orientations of Ta. This difference between yield stresses observed in indentation and SC is attributed to the activation of distinct crystallographic glide mechanisms under varying loading conditions. The complex stress and strain states experienced by crystals during indentation differ significantly from those in compression, thereby resulting in different yield stress behaviors. In particular, the yield stress in indentation is higher than in SC because of the need to activate additional and more difficult to activate slip systems to accommodate the imposed deformation. Moreover, the resulting inhomogeneous deformation causes localized hardening of regions undergoing more straining also contributing to the higher yield stress in indentation. Appendix of the paper presents stress–strain fields for one of the crystals.

Fig. 13 provides a quantitative comparison of the measured and simulated elastic slopes for nanoindentation, complemented with the Young's modulus values for the crystals. The surface plots in this figure aim to visually depict the accuracy in predicting the measured elastic slope values through simulations. Notably, the surface plots representing the measured and simulated values demonstrate a close alignment, appearing nearly flat. In contrast, the surface plot illustrating the Young's modulus values shows noticeable deviations. The deviation in

Table 4
Activated slip systems in the 15 grains in nanoindentation. Also marked are the most active slip system with blue, the second active slip system with green, and the third active slip system with orange.

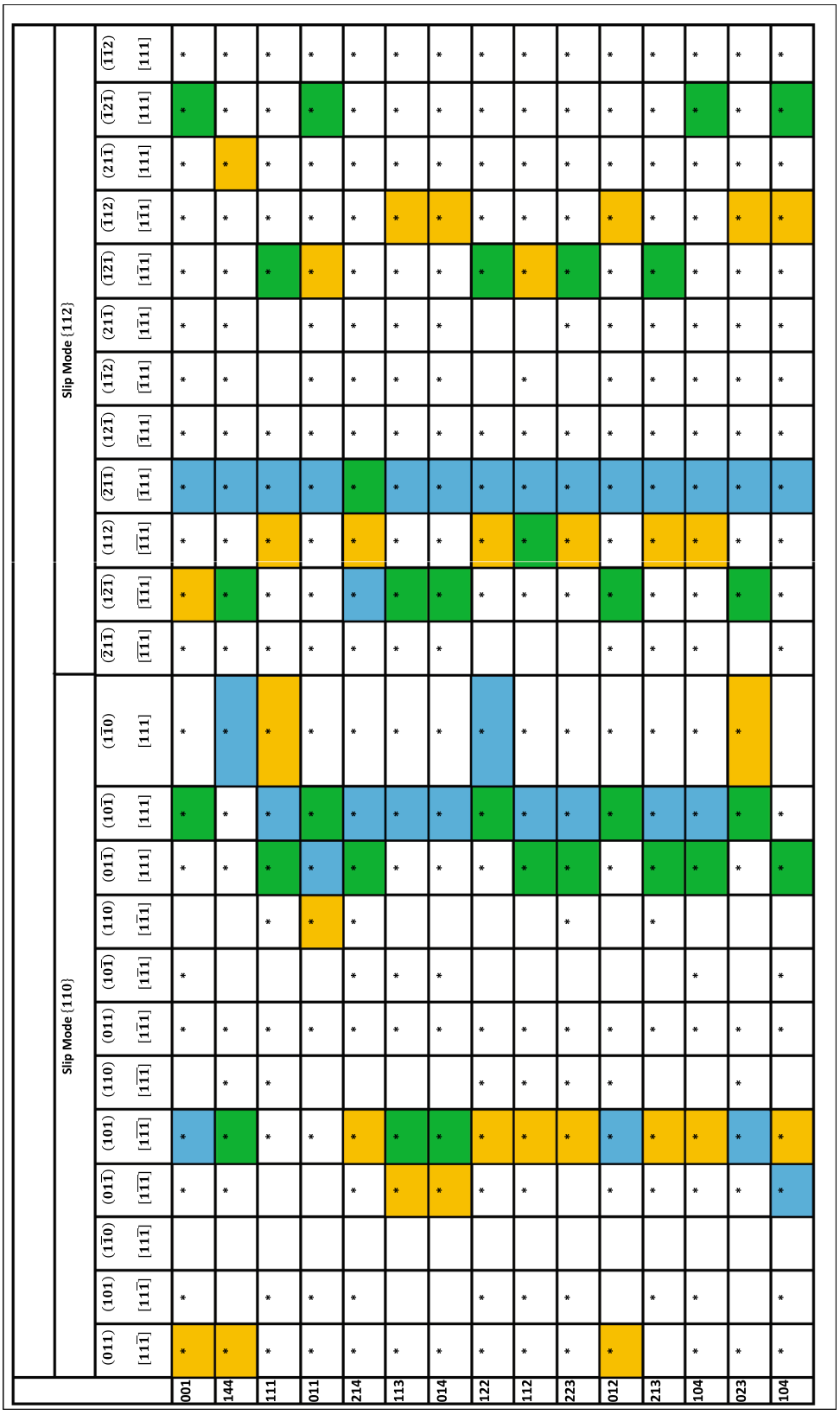

Table 5
Activated slip systems in the 15 grains in simple compression. Also marked are the most active slip system with blue, the second active slip system with green, and the third active slip system with orange.

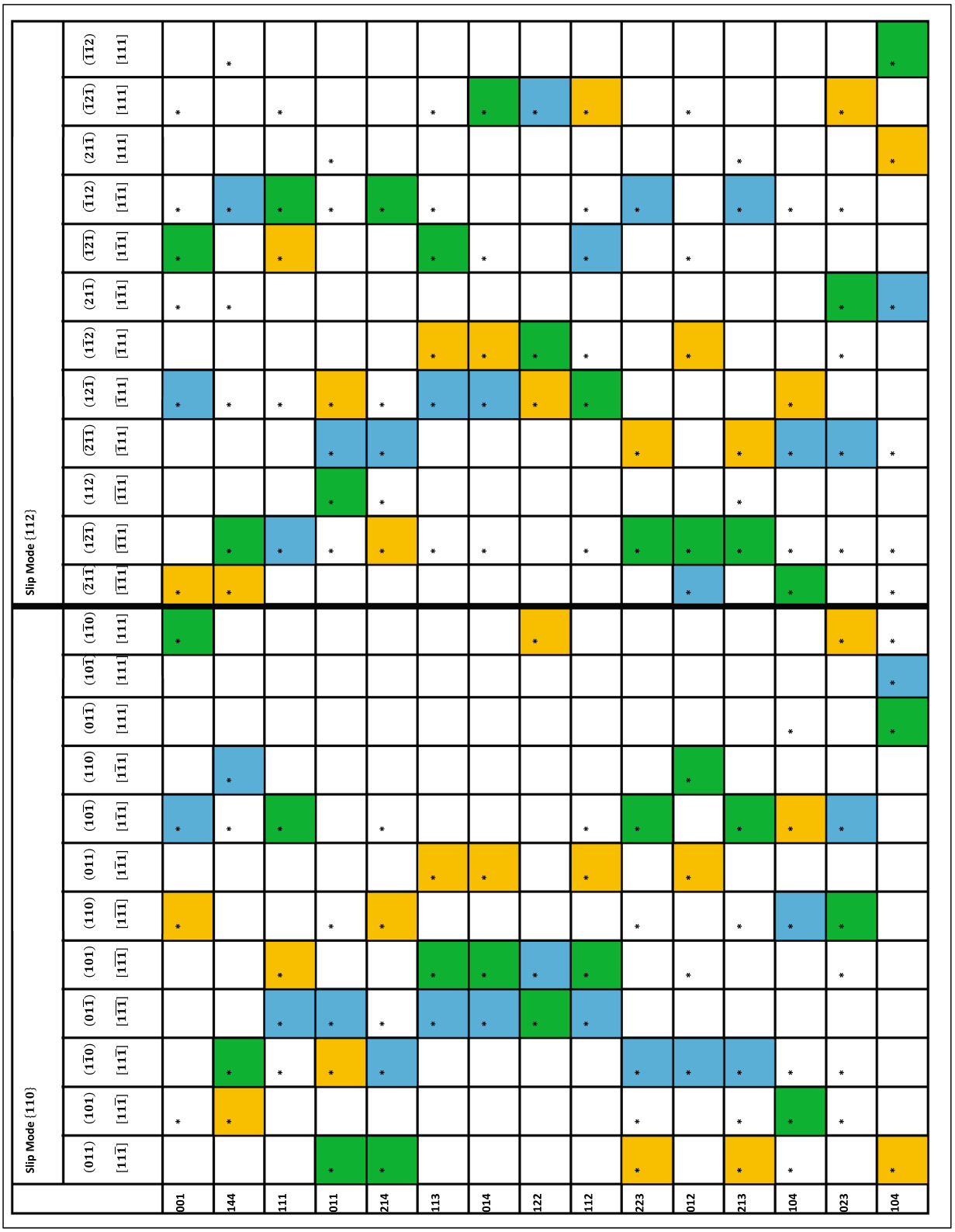

this surface plot is primarily attributed to the approximately 30 GPa gap in elastic slope values for crystal numbers 1 and 14, between the simulated and Young's modulus values.

4. Discussion

An FE model was developed for the simulation of elasto–plastic spherical indentation involving a rigid indenter and a flat deformable specimen of Ta single crystal relying on the CPFE constitutive description. Experiments and corresponding simulations of nanoindentation were used to determine elastic slope, yield stress, and initial hardening per crystal. Moreover, SC simulations were performed for the same crystals to study the differences in compression versus indentation yielding. The model parameters were calibrated using a flow curve obtained in ST. Initial microstructure and texture were characterized using EBSD to initialize the simulations.

Accurate predictions of indentation load–displacement, indentation stress–strain, and yielding of Ta imply that the predicted relative activities of the slip systems contributing to the plastic deformation in indentation and SC are correct. Table 4 and Table 5 list the activated slip systems in indentation and SC, respectively. Appendix A provides the corresponding plots detailing the activities per slip system for all 24 slip systems across two families (12 per family) with strain. The observed variation in yield stresses between indentation and SC lies in the activities of slip systems. The yield stress in indentation is higher than in SC because of the need to activate additional and more difficult to activate slip systems to accommodate the imposed deformation. Moreover, the resulting inhomogeneous deformation causes localized hardening of regions undergoing more straining also contributing to the higher yield stress in indentation than in SC. Owing to the activation of more glide systems in indentation than in SC, the indentation yield stress is less anisotropic than the SC yield stress.

The simulations of both indentation and SC for the same set of Ta crystals allowed us to establish the relationship between conventional yielding and elasticity response obtained in homogeneous uniaxial stress state and yielding and elasticity response in indentation. While the averaged ratio of indentation to SC yield stresses is about 3.1, the range is approximately from 2.6 to 3.6. The variation is owing to the response of individual crystals as driven by their crystallography. The significant role played by crystal orientation-driven anisotropy was recently discussed for Ta single crystals in (Feng et al., 2022).

While we have shown good predictive capabilities of the CPFE model in simulating spherical nanoindentation after been calibrated using the polycrystalline flow stress and texture data, the predictive characteristics of the model can be further improved by calculating geometrically necessary dislocations (GND) and their contribution to hardening and underlying backstress fields. The GNDs have been shown to be important in determining the deformation of crystalline materials under various loadings including indentation using theoretical models (Arsenlis and Parks, 1999; Lu et al., 2020; Nix and Gao, 1998), multiscale simulations (Xu et al., 2019), and experiments (Kysar et al., 2007). Future works will focus on these aspects. Moreover, we will attempt to experimentally verify identified slip systems via slip trace analyses and/or a combination of Digital Image Correlation (DIC) and EBSD.

5. Conclusions

This work adapted and calibrated a crystal plasticity finite element (CPFE) model with dislocation density-based hardening to simulate nanoindentation within the FE framework. Nanoindentation elastic slope and yield stress were measured and simulated for 15 Ta crystals. Moreover, simple compression (SC) simulations were performed for the same crystals. The main conclusions of the combined experimental and modeling study are:

- Successful simulations of spherical nanoindentation showed good predictive capabilities of the CPFE model calibrated using polycrystalline flow stress and texture data to capture the significant role played by crystal orientation-induced anisotropy.
- While the measured and simulated elastic slopes for nanoindentation were in good agreement and not strong functions of crystal orientation, Young's modulus values of the crystals substantially varied.
- The yield stress in indentation was higher than in SC because of the need to activate additional and more difficult to activate slip systems to accommodate the imposed deformation. Inhomogeneous deformation intrinsic to indentation caused localized hardening of regions undergoing more straining, which also contributed to the higher yield stress in indentation. Indentation to compressive yield stress ratios varied with crystal orientation in the range from 2.6 to 3.6.
- Owing to the activation of more glide systems in indentation than in SC, the indentation yield stress was less anisotropic than the SC yield stress.

CRediT authorship contribution statement

Sajjad Izadpanah Najmabad: Methodology, Investigation, Formal analysis. **Olajesu F. Olanrewaju:** Methodology, Investigation, Formal analysis. **Siddhartha Pathak:** Writing – review & editing, Supervision, Resources, Project administration, Methodology, Investigation, Funding acquisition. **Curt A. Bronkhorst:** Writing – review & editing, Supervision, Resources, Project administration, Methodology, Funding acquisition. **Marko Knezevic:** Writing – original draft, Supervision, Software, Resources, Project administration, Methodology, Investigation, Funding acquisition, Formal analysis, Conceptualization.

Declaration of competing interest

The authors declare that they have no known competing financial interests or personal relationships that could have appeared to influence the work reported in this paper.

Data availability

Data will be made available on request.

Acknowledgements

The work presented in this paper was supported by the National Science Foundation under DMREF-2118557 (UNH), -2118673 (ISU), and -2118399 (UW) grant.

Appendix A

The CPFE model is a user material subroutine (UMAT) coupled with Abaqus implicit/standard (Knezevic et al., 2010; Knezevic et al., 2013b). The FE solver of Abaqus iteratively provides guesses of displacement fields at current times, $\tau\,(t+\Delta t)$, under imposed boundary conditions over the mesh. A deformation gradient, $\mathbf{F}$, available at each integration point (IP) is provided to the UMAT at each gauss. The UMAT solves for Cauchy stress, $\boldsymbol{\sigma}$, calculates the Jacobian, and updates state variables to be returned to Abaqus.

The model decomposes $\mathbf{F}$ into its elastic and plastic parts as:

$$\mathbf{F}=\mathbf{F}^{e}\mathbf{F}^{p} \tag{A1}$$

The rate of change of $\mathbf{F}^{p}$ is:

$$\dot{\mathbf{F}}^{p}=\mathbf{L}^{p}\mathbf{F}^{p} \tag{A2}$$

Integrating Eq. (A2) from time at the beginning of the given strain increment, t, to the current time, $\tau=t+\Delta t$, gives:

$$\mathbf{F}^{p}(\tau)=exp(\mathbf{L}^{p}(\tau)\Delta t\,)\mathbf{F}^{p}(t) \tag{A3}$$

The constitutive relations at each IP are:

$$\mathbf{T}=\mathbf{C}\mathbf{E}^{e},\ with\,\mathbf{T}=\mathbf{F}^{e^{-1}}\{(det\mathbf{F}^{e})\boldsymbol{\sigma}\}\mathbf{F}^{e^{-T}}and\ \ \mathbf{E}^{e}=\frac{1}{2}\left\{\mathbf{F}^{e^{T}}\mathbf{F}^{e}-\mathbf{I}\right\} \tag{A4}$$

with $\mathbf{T}$ denoting the second Piola-Kirchhoff stress tensor, $\mathbf{E}^{e}$ denoting the Lagrangian strain tensor, and $\mathbf{C}$ denoting the fourth-rank elastic stiffness tensor. $\mathbf{F}^{e}$ must be known from $\mathbf{F}^{e}(\tau)=\mathbf{F}\mathbf{F}^{p^{-1}}(\tau)=\mathbf{F}\mathbf{F}^{p^{-1}}(t)\{\mathbf{I}-\Delta t\mathbf{L}^{p}(\tau)\}$ to calculate stress. $\mathbf{L}^{p}$ must also be known. Here, $\mathbf{L}$ is additively decomposed to its plastic, $\mathbf{L}^{p}$, and elastic, $\mathbf{L}^{e}$, parts. The former consists of slip shearing contributions as:

$$\mathbf{L}=\mathbf{L}^{e}+\mathbf{L}^{p}=\mathbf{L}^{\mathrm{e}}+\mathbf{L}^{sl}=\mathbf{L}^{e}+\sum_{s}^{N^{sl}}\dot{\gamma}^{s}\mathbf{S}_{0}^{s} \tag{A5}$$

In Eq. (A5), $\mathbf{S}_{0}^{s}=\mathbf{b}_{0}^{s}\otimes\mathbf{n}_{0}^{s}$ are Schmid tensors for slip systems, s, in their reference configuration denoted with $_0$. These Schmid tensors are based on $\mathbf{b}_{0}^{s}$ Burgers vectors and $\mathbf{n}_{0}^{s}$ plane normal vectors. $\dot{\gamma}^{s}$ is the rate of shearing.

The Schmid resolved shear stress for activation of a slip system is modified by adding the non-Schmid effects/projections as (Dao and Asaro, 1993; Knezevic et al., 2014a; Lim et al., 2013; Savage et al., 2017; Savage et al., 2018):

$$\tau^{s}=\mathbf{S}_{0}^{s}\bullet\mathbf{T}+\mathbf{P}_{ns}^{s}\bullet\mathbf{T}=\mathbf{P}_{tot}^{s}\bullet\mathbf{T} \tag{A6}$$

where the non-Schmid tensor is a weighted sum of the following five dyads:

$$\mathbf{P}_{ns}^{s}=c_{1}\left(\mathbf{t}_{0}^{s}\otimes\mathbf{b}_{0}^{s}\right)+c_{2}\left(\mathbf{t}_{0}^{s}\otimes\mathbf{n}_{0}^{s}\right)+c_{3}\left(\mathbf{n}_{0}^{s}\otimes\mathbf{n}_{0}^{s}\right)+c_{4}\left(\mathbf{t}_{0}^{s}\otimes\mathbf{t}_{0}^{s}\right)-\left(c_{3}+c_{4}\right)\left(\mathbf{b}_{0}^{s}\otimes\mathbf{b}_{0}^{s}\right) \tag{A7}$$

In Eq. (A7), $\mathbf{t}^{s}$ is a unit vector in the glide plane but perpendicular to the slip direction, $\mathbf{t}^{s}=\mathbf{n}^{s}\times\mathbf{b}^{s}$ and c_i are the weighting non-Schmid coefficients. These coefficients for Ta at room temperature reported in (Lim et al., 2013): $c_1=-0.15, c_2=0.13, c_3=-0.07, c_4=0.04$ are used in the present work like in several other studies (Knezevic et al., 2014a; Zecevic and Knezevic, 2018). Finally, the power-law equation for slip systems is (Asaro and Needleman, 1985; Hutchinson, 1976; Kalidindi, 1998; Knezevic et al., 2016; Vasilev et al., 2020; Zecevic et al., 2016).

$$\dot{\gamma}^{s}=\dot{\gamma}_{0}\left(\frac{\tau^{s}}{\tau_{\mathrm{c}}^{s}}\right)^{\frac{1}{\mathrm{m}}}with\tau^{s}<0\rightarrow\dot{\gamma}^{s}=0 \tag{A8}$$

where $\dot{\gamma}_0$ is a reference value for shearing rate ($\dot{\gamma}_0=0.001\mathrm{s}^{-1}$), τ^{s} is the resolved shear stress on system s, τ_c^{s} is a threshold value to slip defined shortly, and $\frac{1}{\mathrm{m}}$ is the power-law exponent with m representing a strain-rate sensitivity. The exponent, $\frac{1}{m}=n=20$, is appropriate for Ta (Feng et al., 2022; Knezevic et al., 2014a). Note that positive and negative slip directions are considered separately.

Appendix B

This appendix presents stress–strain fields for one of the crystals (Figure B1) and relative activities of slip systems activated in nanoindentation (Figure B2) and simple compression (Figure B3).

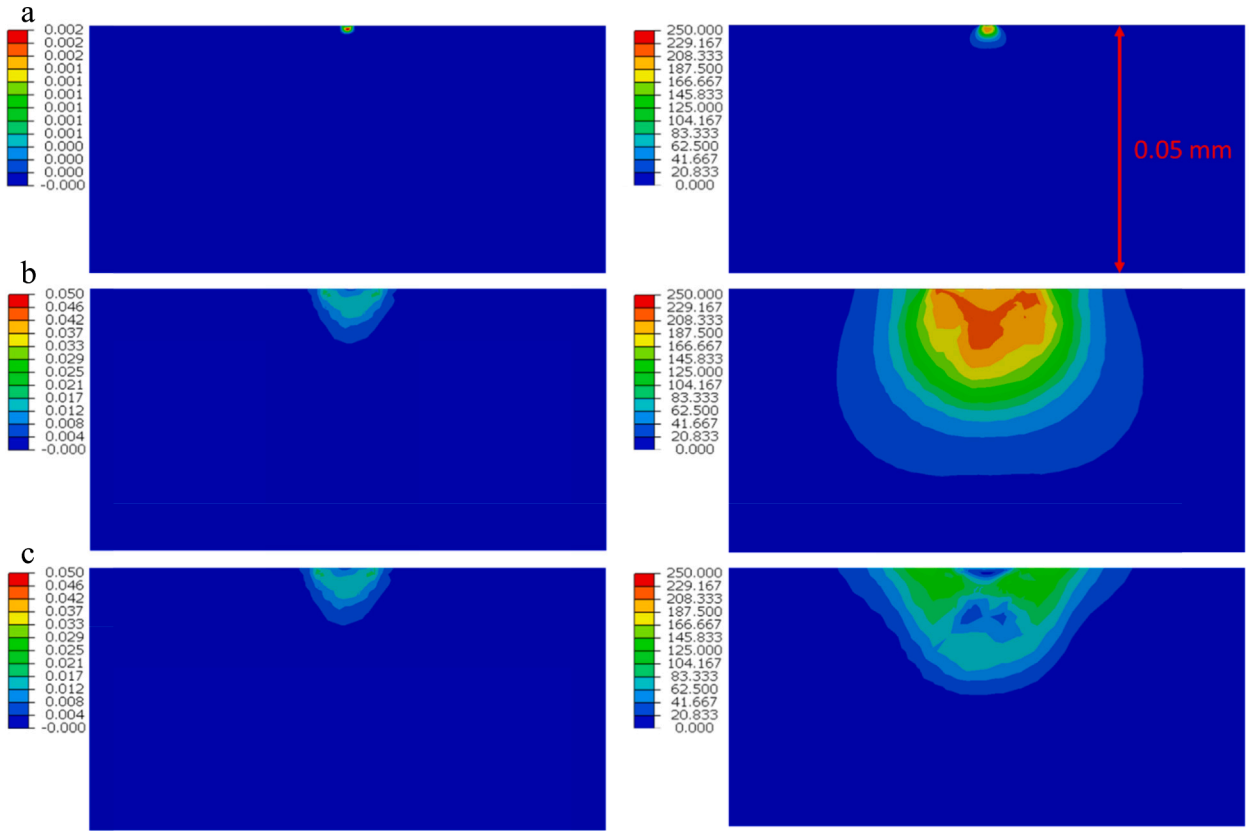

Fig. B1. Effective strain fields (left) and von Mises stress fields (right) underneath the indenter sectioned through the middle YX plane of the model during the indentation of (0 0 1) crystal orientation: (a) at yield, (b) end of indentation, and (c) after retracting the indenter.

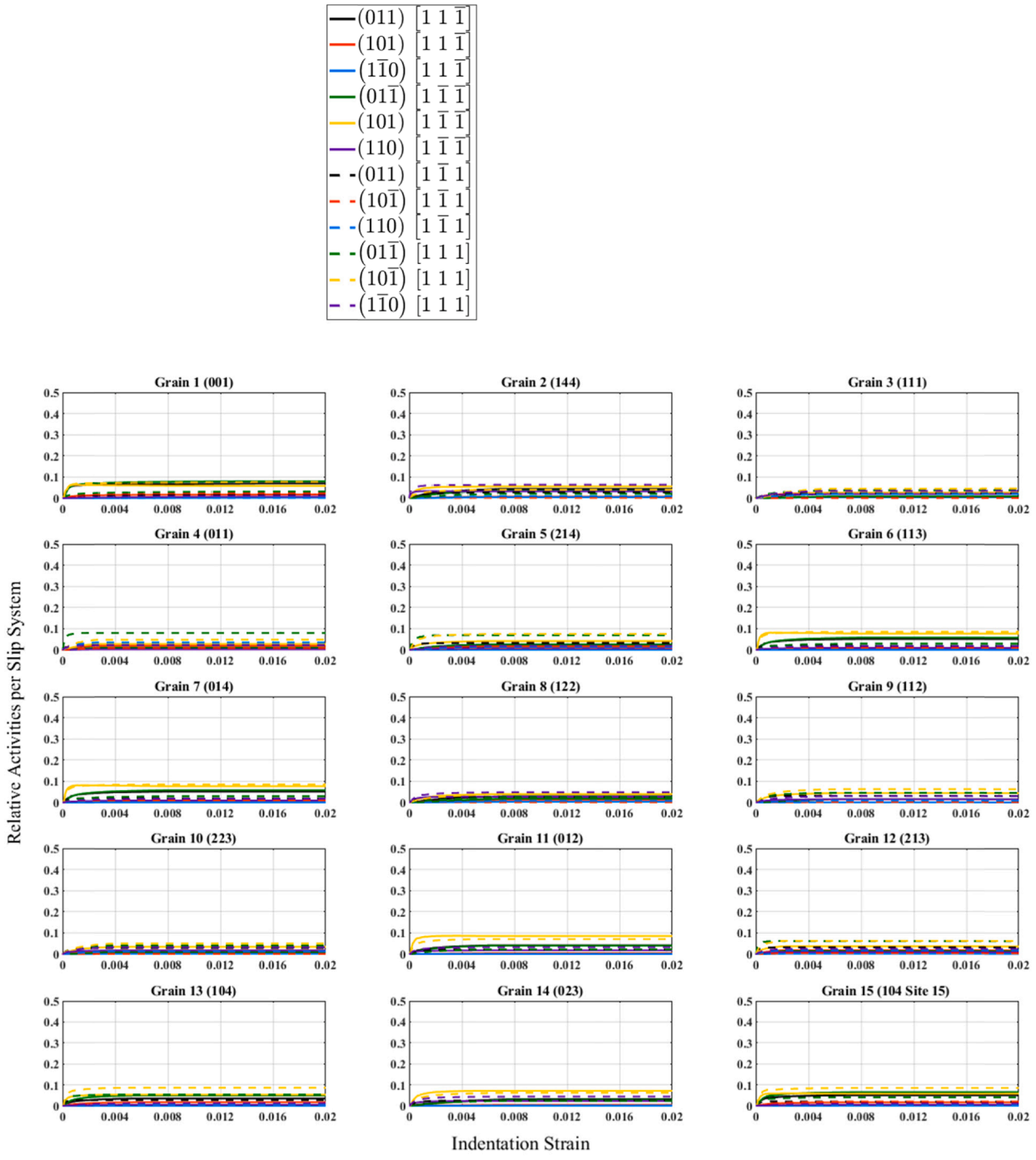

Fig. B2. Predicted relative activities of each slip system in (a) mode and (b) mode accommodating the plasticity in nanoindentation of the 15 grains.

b

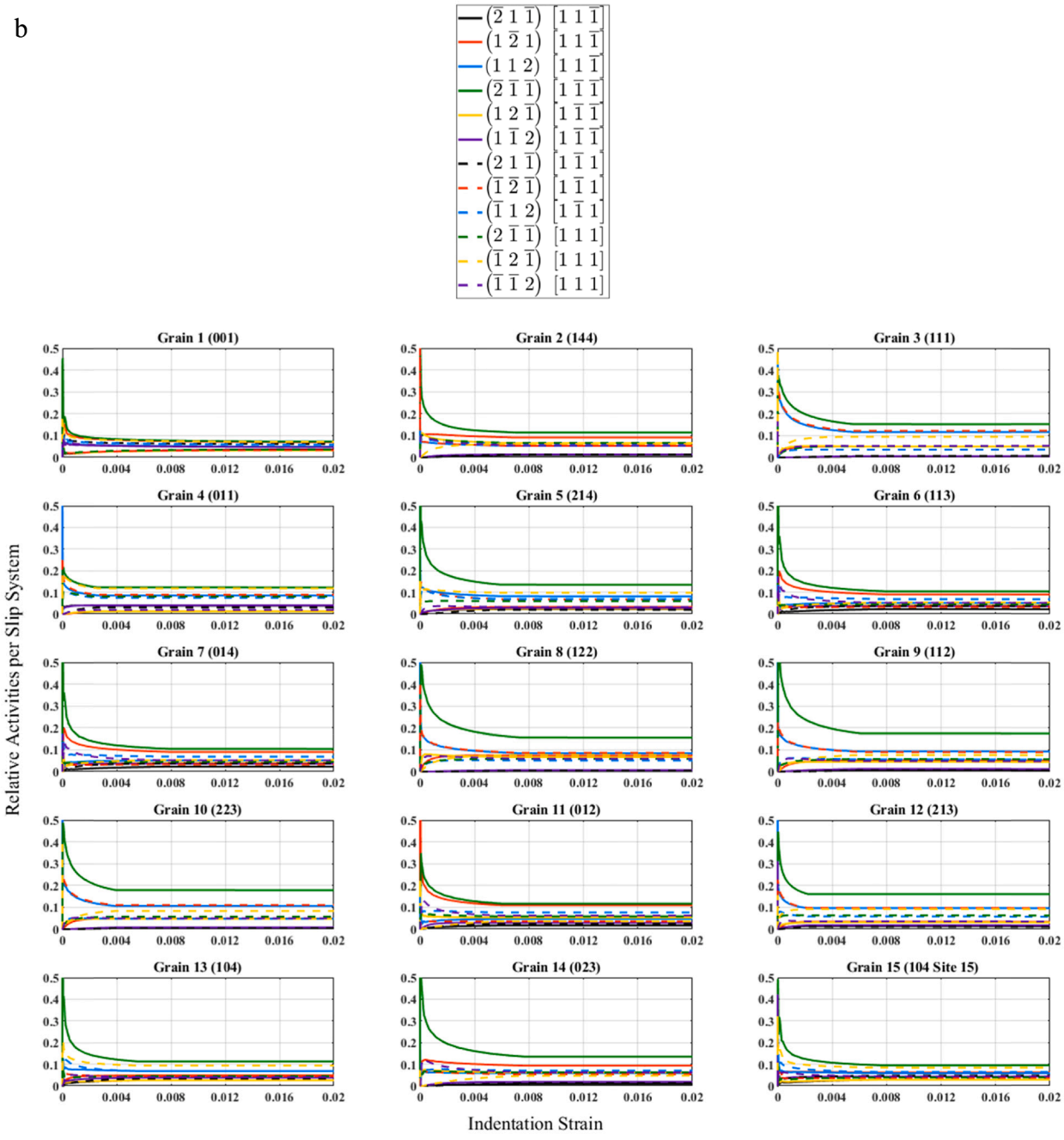

Fig. B2. (*continued*).

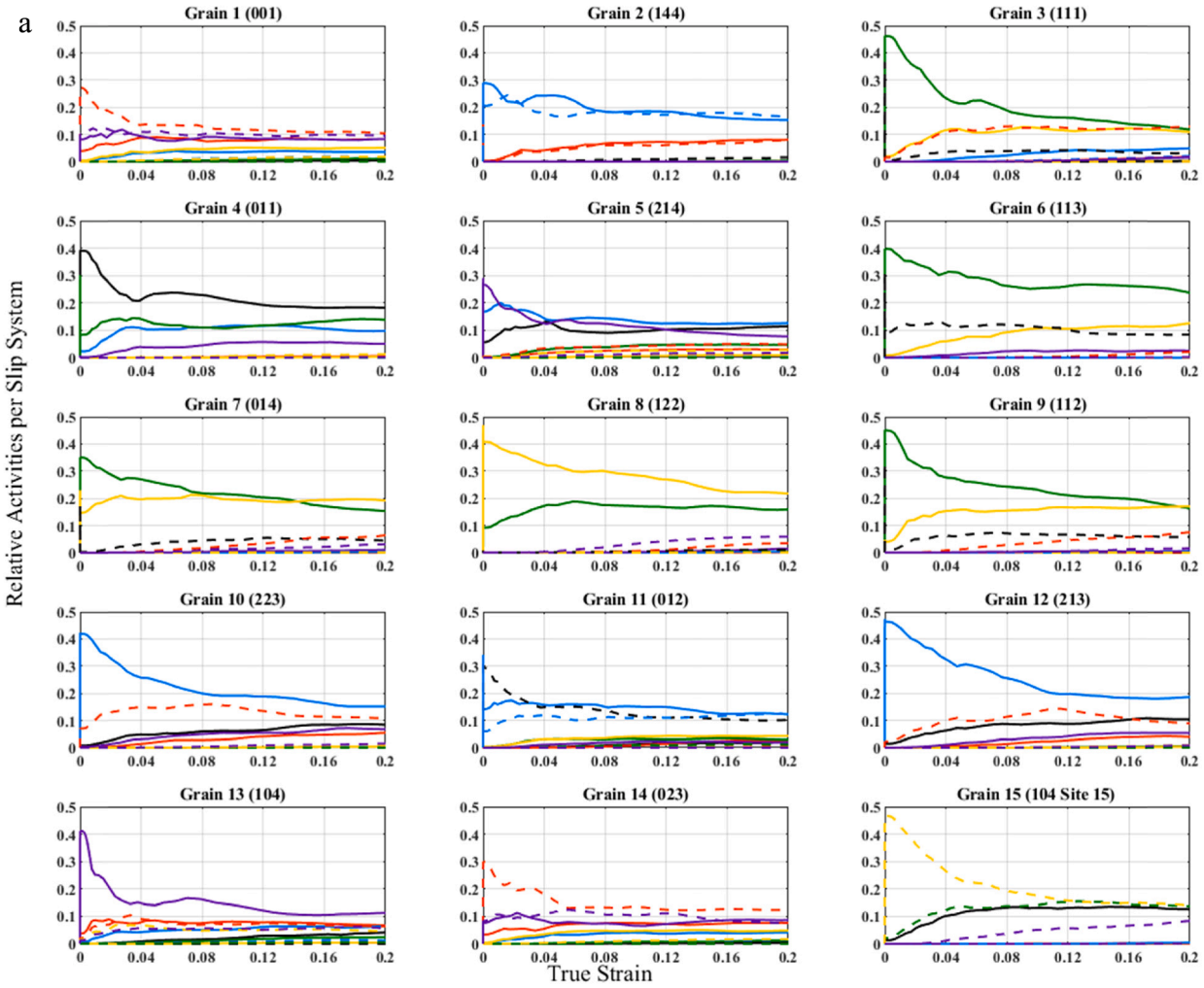

Fig. B3. Predicted relative activities of each slip system in (a) mode and (b) mode accommodating the plasticity in simple compression of the 15 grains. Legends are the same as in Figure B2.

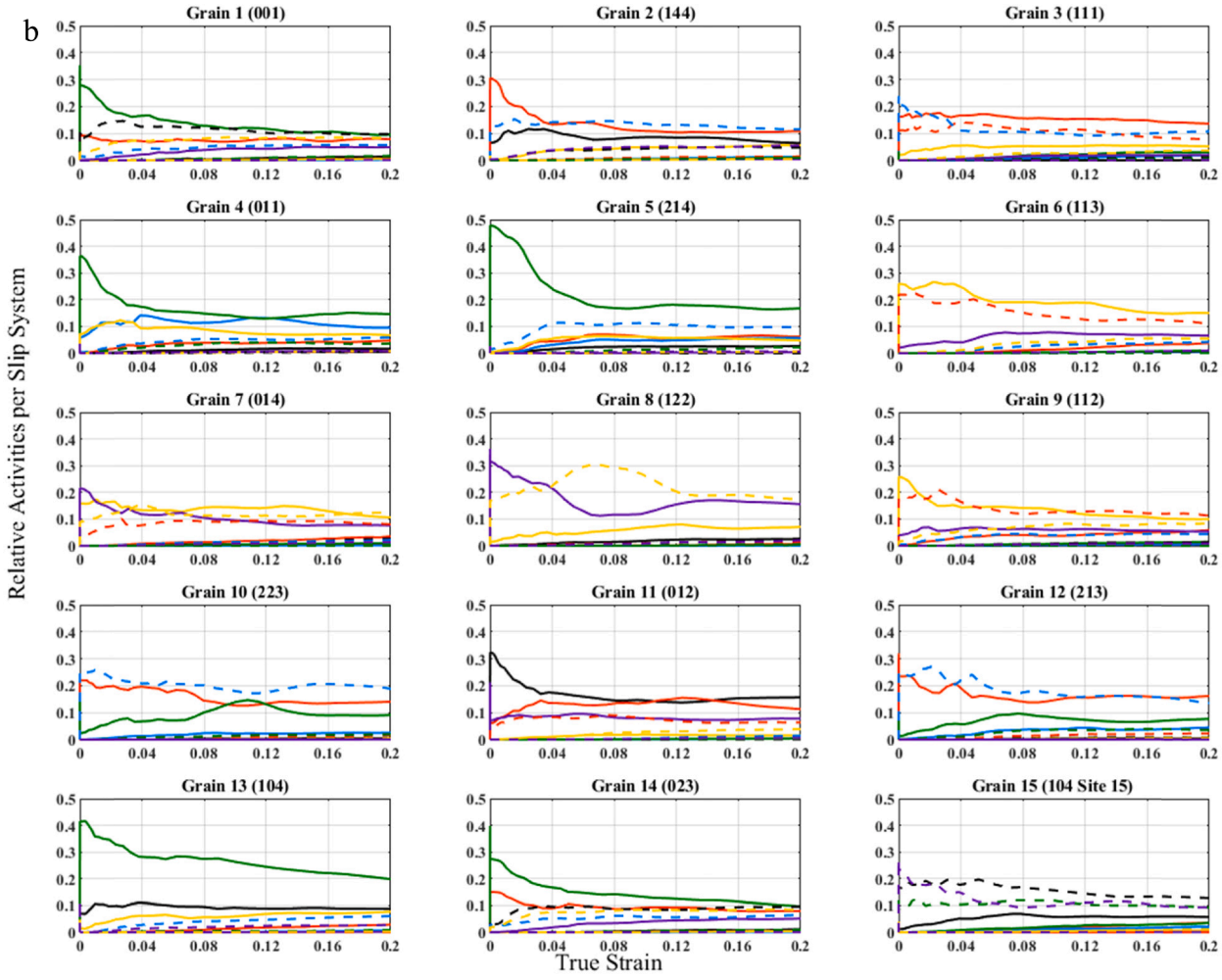

Fig. B3. (*continued*).

References

Al-Harbi, H.F., Knezevic, M., Kalidindi, S.R., 2010. Spectral approaches for the fast computation of yield surfaces and first-order plastic property closures for polycrystalline materials with cubic-triclinic textures. CMC: Computers Materials, & Continua 15, 153–172.

Ardeljan, M., Beyerlein, I.J., McWilliams, B.A., Knezevic, M., 2016a. Strain rate and temperature sensitive multi-level crystal plasticity model for large plastic deformation behavior: Application to AZ31 magnesium alloy. Int. J. Plast. 83, 90–109.

Ardeljan, M., Beyerlein, I.J., Knezevic, M., 2017. Effect of dislocation density-twin interactions on twin growth in AZ31 as revealed by explicit crystal plasticity finite element modeling. Int. J. Plast.

Ardeljan, M., Knezevic, M., 2018. Explicit modeling of double twinning in AZ31 using crystal plasticity finite elements for predicting the mechanical fields for twin variant selection and fracture analyses. Acta. Mater. 157, 339–354.

Ardeljan, M., Knezevic, M., Nizolek, T., Beyerlein, I.J., Mara, N.A., Pollock, T.M., 2015a. A study of microstructure-driven strain localizations in two-phase polycrystalline HCP/BCC composites using a multi-scale model. Int. J. Plast. 74, 35–57.

Ardeljan, M., McCabe, R.J., Beyerlein, I.J., Knezevic, M., 2015b. Explicit incorporation of deformation twins into crystal plasticity finite element models. Comput. Methods Appl. Mech. Eng. 295, 396–413.

Ardeljan, M., Savage, D.J., Kumar, A., Beyerlein, I.J., Knezevic, M., 2016b. The plasticity of highly oriented nano-layered Zr/Nb composites. Acta. Mater. 115, 189–203.

Arsenlis, A., Parks, D.M., 1999. Crystallographic aspects of geometrically-necessary and statistically-stored dislocation density. Acta. Mater. 47, 1597–1611.

Asaro, R.J., Needleman, A., 1985. Texture development and strain hardening in rate dependent polycrystals. Acta Metall. Mater. 33, 923–953.

Beghini, M., Bertini, L., Fontanari, V., 2006. Evaluation of the stress–strain curve of metallic materials by spherical indentation. Int. J. Solids Struct. 43, 2441–2459.

Beyerlein, I.J., Tomé, C.N., 2008. A dislocation-based constitutive law for pure Zr including temperature effects. Int. J. Plast. 24, 867–895.

Bhattacharyya, A., Knezevic, M., Abouaf, M., 2015. Characterization of crystallographic texture and intra-grain morphology in cross-rolled tantalum. Metall. Mater. Trans. A 46, 1085–1096.

Bronkhorst, C.A., Gray III, G.T., Addessio, F.L., Livescu, V., Bourne, N., McDonald, S., Withers, P., 2016. Response and representation of ductile damage under varying shock loading conditions in tantalum. J. Appl. Phys. 119, 085103.

Buckman, R.W., 2000. New applications for tantalum and tantalum alloys. JOM 52, 40–41.

Cantara, A.M., Zecevic, M., Eghtesad, A., Poulin, C.M., Knezevic, M., 2019. Predicting elastic anisotropy of dual-phase steels based on crystal mechanics and microstructure. Int. J. Mech. Sci. 151, 639–649.

Capolungo, L., Beyerlein, I.J., Tomé, C.N., 2009. Slip-assisted twin growth in hexagonal close-packed metals. Scr. Mater. 60, 32–35.

Chen, S., Gray, G., 1996. Constitutive behavior of tantalum and tantalum-tungsten alloys. Metall. Mater. Trans. A 27, 2994–3006.

Christian, J., 1983. Some surprising features of the plastic deformation of body-centered cubic metals and alloys. Metall. Mater. Trans. A 14, 1237–1256.

Dao, M., Asaro, R.J., 1993. Non-Schmid effects and localized plastic flow in intermetallic alloys. Mater. Sci. Eng. A 170, 143–160.

Donohue, B.R., Ambrus, A., Kalidindi, S.R., 2012. Critical evaluation of the indentation data analyses methods for the extraction of isotropic uniaxial mechanical properties using finite element models. Acta. Mater. 60, 3943–3952.

Fabricated Products High Performance Solutions. H.C. Starck Inc., 2013.

Fast, T., Knezevic, M., Kalidindi, S.R., 2008. Application of microstructure sensitive design to structural components produced from hexagonal polycrystalline metals. Comput. Mater. Sci. 43, 374–383.

Feather, W.G., Ghorbanpour, S., Savage, D.J., Ardeljan, M., Jahedi, M., McWilliams, B.A., Gupta, N., Xiang, C., Vogel, S.C., Knezevic, M., 2019. Mechanical response, twinning, and texture evolution of WE43 magnesium-rare earth alloy as a function of strain rate: experiments and multi-level crystal plasticity modeling. Int. J. Plast. 120, 180–204.

Feather, W.G., Lim, H., Knezevic, M., 2020. A numerical study into element type and mesh resolution for crystal plasticity finite element modeling of explicit grain structures. Comput. Mech.
Feather, W.G., Savage, D.J., Knezevic, M., 2021. A crystal plasticity finite element model embedding strain-rate sensitivities inherent to deformation mechanisms: application to alloy AZ31. Int. J. Plast. 143, 103031.
Feng, Z., Yoon, S.-Y., Choi, J.-H., Barrett, T.J., Zecevic, M., Barlat, F., Knezevic, M., 2020. A comparative study between elasto-plastic self-consistent crystal plasticity and anisotropic yield function with distortional hardening formulations for sheet metal forming. Mech. Mater. 148, 103422.
Feng, Z., Zecevic, M., Knezevic, M., Lebensohn, R.A., 2022. Predicting extreme anisotropy and shape variations in impact testing of tantalum single crystals. Int. J. Solids Struct. 241, 111466.
Fischer-Cripps, A.C., 2000. A review of analysis methods for sub-micron indentation testing. Vacuum 58, 569–585.
Fischer-Cripps, A.C., Nicholson, D., 2004. Nanoindentation. Mech. Eng. Series. Appl. Mech. Rev. 57, B12–B.
Hertz, H., 1896. Miscellaneous Papers. MacMillan and Co., Ltd., New York.
Hesla, L., 2011. Seamless cavity performance. International Linear Collider Newsline.
Hoge, K., Mukherjee, A., 1977. The temperature and strain rate dependence of the flow stress of tantalum. J. Mater. Sci. 12, 1666–1672.
Hutchinson, J.W., 1976. Bounds and self-consistent estimates for creep of polycrystalline materials. Proceedings of the Royal Society of London. Series A, Mathematical and Physical Sciences 348, 101-126.
Kalidindi, S.R., 1998. Incorporation of deformation twinning in crystal plasticity models. J. Mech. Phys. Solids 46, 267–271.
Kalidindi, S.R., Bronkhorst, C.A., Anand, L., 1992. Crystallographic texture evolution in bulk deformation processing of FCC metals. J. Mech. Phys. Solids 40, 537–569.
Kalidindi, S.R., Pathak, S., 2008. Determination of the effective zero-point and the extraction of spherical nanoindentation stress–strain curves. Acta. Mater. 56, 3523–3532.
Knezevic, M., Beyerlein, I.J., 2018. Multiscale modeling of microstructure-property relationships of polycrystalline metals during thermo-mechanical deformation. Adv. Eng. Mater. 20, 1700956.
Knezevic, M., Beyerlein, I.J., Brown, D.W., Sisneros, T.A., Tomé, C.N., 2013a. A polycrystal plasticity model for predicting mechanical response and texture evolution during strain-path changes: application to beryllium. Int. J. Plast. 49, 185–198.
Knezevic, M., Beyerlein, I.J., Lovato, M.L., Tomé, C.N., Richards, A.W., McCabe, R.J., 2014a. A strain-rate and temperature dependent constitutive model for BCC metals incorporating non-Schmid effects: application to tantalum–tungsten alloys. Int. J. Plast. 62, 93–104.
Knezevic, M., Carpenter, J.S., Lovato, M.L., McCabe, R.J., 2014b. Deformation behavior of the cobalt-based superalloy Haynes 25: experimental characterization and crystal plasticity modeling. Acta. Mater. 63, 162–168.
Knezevic, M., Drach, B., Ardeljan, M., Beyerlein, I.J., 2014c. Three dimensional predictions of grain scale plasticity and grain boundaries using crystal plasticity finite element models. Comput. Methods Appl. Mech. Eng. 277, 239–259.
Knezevic, M., Kalidindi, S.R., 2007. Fast computation of first-order elastic-plastic closures for polycrystalline cubic-orthorhombic microstructures. Comput. Mater. Sci. 39, 643–648.
Knezevic, M., Kalidindi, S.R., Fullwood, D., 2008a. Computationally efficient database and spectral interpolation for fully plastic Taylor-type crystal plasticity calculations of face-centered cubic polycrystals. Int. J. Plast. 24, 1264–1276.
Knezevic, M., Kalidindi, S.R., Mishra, R.K., 2008b. Delineation of first-order closures for plastic properties requiring explicit consideration of strain hardening and crystallographic texture evolution. Int. J. Plast. 24, 327–342.
Knezevic, M., Al-Harbi, H.F., Kalidindi, S.R., 2009. Crystal plasticity simulations using discrete Fourier transforms. Acta. Mater. 57, 1777–1784.
Knezevic, M., Levinson, A., Harris, R., Mishra, R.K., Doherty, R.D., Kalidindi, S.R., 2010. Deformation twinning in AZ31: Influence on strain hardening and texture evolution. Acta. Mater. 58, 6230–6242.
Knezevic, M., Capolungo, L., Tomé, C.N., Lebensohn, R.A., Alexander, D.J., Mihaila, B., McCabe, R.J., 2012. Anisotropic stress-strain response and microstructure evolution of textured α-uranium. Acta. Mater. 60, 702–715.
Knezevic, M., McCabe, R.J., Lebensohn, R.A., Tomé, C.N., Liu, C., Lovato, M.L., Mihaila, B., 2013b. Integration of self-consistent polycrystal plasticity with dislocation density based hardening laws within an implicit finite element framework: application to low-symmetry metals. J. Mech. Phys. Solids 61, 2034–2046.
Knezevic, M., McCabe, R.J., Tomé, C.N., Lebensohn, R.A., Chen, S.R., Cady, C.M., Gray Iii, G.T., Mihaila, B., 2013c. Modeling mechanical response and texture evolution of α-uranium as a function of strain rate and temperature using polycrystal plasticity. Int. J. Plast. 43, 70–84.
Knezevic, M., Zecevic, M., Beyerlein, I.J., Bhattacharyya, A., McCabe, R.J., 2015. Predicting texture evolution in Ta and Ta-10W alloys using polycrystal plasticity. JOM 67, 2670–2674.
Knezevic, M., Zecevic, M., Beyerlein, I.J., Lebensohn, R.A., 2016. A numerical procedure enabling accurate descriptions of strain rate-sensitive flow of polycrystals within crystal visco-plasticity theory. Comput. Methods Appl. Mech. Eng. 308, 468–482.
Kocks, U.F., Mecking, H., 2003. Physics and phenomenology of strain hardening: the FCC case. Prog. Mater. Sci. 48, 171–273.
Kocks, U.F., Tomé, C.N., Wenk, H.-R., 1998. Texture and Anisotropy. Cambridge University Press, Cambridge, UK.
Kysar, J.W., Gan, Y.X., Morse, T.L., Chen, X., Jones, M.E., 2007. High strain gradient plasticity associated with wedge indentation into face-centered cubic single crystals: geometrically necessary dislocation densities. J. Mech. Phys. Solids 55, 1554–1573.
Lim, H., Weinberger, C.R., Battaile, C.C., Buchheit, T.E., 2013. Application of generalized non-Schmid yield law to low-temperature plasticity in bcc transition metals. Model. Simul. Mater. Sci. Eng. 21, 045015.
Lu, X., Dunne, F.P.E., Xu, Y., 2020. A crystal plasticity investigation of slip system interaction, GND density and stored energy in non-proportional fatigue in Nickel-based superalloy. Int. J. Fatigue 139, 105782.
Mathur, K.K., Dawson, P.R., 1989. On modelling the development of crystallographic texture in bulk forming processes. Int. J. Plast. 5, 67–94.
Matsuno, H., Yokoyama, A., Watari, F., Uo, M., Kawasaki, T., 2001. Biocompatibility and osteogenesis of refractory metal implants, titanium, hafnium, niobium, tantalum and rhenium. Biomaterials 22, 1253–1262.
Meyers, M.A., Chawla, K.K., 2009. Chapter 2. Elasticity and Viscoelasticity, Mechanical Behavior of Materials. Cambridge University Press.
Nix, W.D., Gao, H., 1998. Indentation size effects in crystalline materials: A law for strain gradient plasticity. J. Mech. Phys. Solids 46, 411–425.
Patel, D.K., Kalidindi, S.R., 2016. Correlation of spherical nanoindentation stress-strain curves to simple compression stress-strain curves for elastic-plastic isotropic materials using finite element models. Acta. Mater. 112, 295–302.
Patel, D.K., Kalidindi, S.R., 2017. Estimating the slip resistance from spherical nanoindentation and orientation measurements in polycrystalline samples of cubic metals. Int. J. Plast. 92, 19–30.
Pathak, S., Kalidindi, S.R., 2015. Spherical nanoindentation stress–strain curves. Mater. Sci. Eng. R. Rep. 91, 1–36.
Pathak, S., Stojakovic, D., Doherty, R., Kalidindi, S.R., 2009a. Importance of surface preparation on the nano-indentation stress-strain curves measured in metals. Journal of Materials Research - Focus Issue on Indentation Methods in Advanced Materials Research 24, 1142–1155.
Pathak, S., Stojakovic, D., Kalidindi, S.R., 2009b. Measurement of the local mechanical properties in polycrystalline samples using spherical nanoindentation and orientation imaging microscopy. Acta. Mater. 57, 3020–3028.
Pelletier, H., 2006. Predictive model to estimate the stress–strain curves of bulk metals using nanoindentation. Tribol. Int. 39, 593–606.
Savage, D.J., Beyerlein, I.J., Knezevic, M., 2017. Coupled texture and non-Schmid effects on yield surfaces of body-centered cubic polycrystals predicted by a crystal plasticity finite element approach. Int. J. Solids Struct. 109, 22–32.
Savage, D.J., Chandola, N., Cazacu, O., McWilliams, B.A., Knezevic, M., 2018. Validation of recent analytical dilatational models for porous polycrystals using crystal plasticity finite element models with Schmid and non-Schmid activation laws. Mech. Mater. 126, 148–162.
Savage, D.J., Feng, Z., Knezevic, M., 2021. Identification of crystal plasticity model parameters by multi-objective optimization integrating microstructural evolution and mechanical data. Comput. Methods Appl. Mech. Eng. 379, 113747.
Shaffer, J.B., Knezevic, M., Kalidindi, S.R., 2010. Building texture evolution networks for deformation processing of polycrystalline fcc metals using spectral approaches: applications to process design for targeted performance. Int. J. Plast. 26, 1183–1194.
Shields Jr, J., Lipetzky, P., Mueller, A., 1999. Fracture Toughness of 6.4 mm arc-cast molybdenum and molybdenum-TZM plate at room temperature and 300 deg C, DE-AC11-98PN38206.
Taljat, B., Zacharia, T., Kosel, F., 1998. New analytical procedure to determine stress-strain curve from spherical indentation data. Int. J. Solids Struct. 35, 4411–4426.
Vasilev, E., Zecevic, M., McCabe, R.J., Knezevic, M., 2020. Experimental verification of a crystal plasticity-based simulation framework for predicting microstructure and geometric shape changes: application to bending and Taylor impact testing of Zr. Int. J. Impact Eng 144, 103655.
Veasna, K., Feng, Z., Zhang, Q., Knezevic, M., 2023. Machine learning-based multi-objective optimization for efficient identification of crystal plasticity model parameters. Comput. Methods Appl. Mech. Eng. 403, 115740.
Vlassak, J.J., Nix, W.D., 1993. Indentation modulus of elastically anisotropic half spaces. Philosophical Magazine A (Physics of Condensed Matter, Defects and Mechanical Properties) 67, 1045–1056.
Vlassak, J.J., Nix, W.D., 1994. Measuring the elastic properties of anisotropic materials by means of indentation experiments. J. Mech. Phys. Solids 42, 1223–1245.
Weaver, J.S., Kalidindi, S.R., 2016. Mechanical characterization of Ti-6Al-4V titanium alloy at multiple length scales using spherical indentation stress-strain measurements. Mater. Des. 111, 463–472.
Weaver, J.S., Priddy, M.W., McDowell, D.L., Kalidindi, S.R., 2016. On capturing the grain-scale elastic and plastic anisotropy of alpha-Ti with spherical nanoindentation and electron back-scattered diffraction. Acta. Mater. 117, 23–34.
Weiss, J., Knezevic, M., 2024. Effects of element type on accuracy of microstructural mesh crystal plasticity finite element simulations and comparisons with elasto-viscoplastic fast Fourier transform predictions. Comput. Mater. Sci. 240, 113002.
Weiss, J., Su, Y., McWilliams, B.A., Beyerlein, I.J., Knezevic, M., 2023. Embedding strain-rate sensitivities of multiple deformation mechanisms to predict the behavior of a precipitate-hardened WE43 alloy under a wide range of strain rates. Mech. Mater. 187, 104843.
Weiss, J., Savage, D.J., Knezevic, M., 2024. A parametric study into the influence of Taylor-type scale-bridging artifacts on accuracy of multi-level crystal plasticity finite element models for Mg alloys. Comput. Mater. Sci. 232, 112684.
Wu, X., Proust, G., Knezevic, M., Kalidindi, S.R., 2007. Elastic-plastic property closures for hexagonal close-packed polycrystalline metals using first-order bounding theories. Acta. Mater. 55, 2729–2737.

Xu, Y., Balint, D.S., Dini, D., 2019. A new hardness formula incorporating the effect of source density on indentation response: a discrete dislocation plasticity analysis. Surf. Coat. Technol. 374, 763–773.
Xu, Y., Gu, T., Xian, J., Giuliani, F., Ben Britton, T., Gourlay, C.M., Dunne, F.P.E., 2022. Multi-scale plasticity homogenization of Sn–3Ag-0.5Cu: from β-Sn micropillars to polycrystals with intermetallics. Mater. Sci. Eng. A 855, 143876.
Zecevic, M., Beyerlein, I.J., McCabe, R.J., McWilliams, B.A., Knezevic, M., 2016. Transitioning rate sensitivities across multiple length scales: microstructure-property relationships in the Taylor cylinder impact test on zirconium. Int. J. Plast. 84, 138–159.
Zecevic, M., Beyerlein, I.J., Knezevic, M., 2017. Coupling elasto-plastic self-consistent crystal plasticity and implicit finite elements: applications to compression, cyclic tension-compression, and bending to large strains. Int. J. Plast. 93, 187–211.
Zecevic, M., Upadhyay, M.V., Polatidis, E., Panzner, T., Van Swygenhoven, H., Knezevic, M., 2019. A crystallographic extension to the Olson-Cohen model for predicting strain path dependence of martensitic transformation. Acta. Mater. 166, 386–401.
Zecevic, M., Cawkwell, M.J., Ramos, K.J., Luscher, D.J., 2021. Simulating Knoop hardness anisotropy of aluminum and β-HMX with a crystal plasticity finite element model. Int. J. Plast. 144, 103045.
Zecevic, M., Knezevic, M., 2015. A dislocation density based elasto-plastic self-consistent model for the prediction of cyclic deformation: application to Al6022-T4. Int. J. Plast. 72, 200–217.
Zecevic, M., Knezevic, M., 2017. Modeling of sheet metal forming based on implicit embedding of the elasto-plastic self-consistent formulation in shell elements: application to cup drawing of AA6022-T4. JOM 69, 922–929.
Zecevic, M., Knezevic, M., 2018. A new visco-plastic self-consistent formulation implicit in dislocation-based hardening within implicit finite elements: application to high strain rate and impact deformation of tantalum. Comput. Methods Appl. Mech. Eng. 341, 888–916.
Zecevic, M., Knezevic, M., McWilliams, B., Lebensohn, R.A., 2020. Modeling of the thermo-mechanical response and texture evolution of WE43 Mg alloy in the dynamic recrystallization regime using a viscoplastic self-consistent formulation. Int. J. Plast. 130, 102705.
Zhang, Z., Jun, T.-S., Britton, T.B., Dunne, F.P.E., 2016. Intrinsic anisotropy of strain rate sensitivity in single crystal alpha titanium. Acta. Mater. 118, 317–330.